Published OnlineFirst October 31, 2011; DOI:10.1158/0008-5472.CAN-11-1758

Fig. S6), but we observed no papillomas or SCC at any time in K14-*Angptl2* Tg or wild-type mice treated with DMBA only or PMA only (data not shown), indicating that Angptl2 overexpression cannot cause a "preneoplastic change." At 8 weeks after beginning chemical treatment of both DMBA and PMA, numerous papillomas were detected in K14-*Angptl2* Tg, whereas only a few were seen in wild-type mice (Fig. 1A). K14-*Angptl2* Tg also showed accelerated formation of skin papillomas, with an average latency of 7 weeks after the beginning of chemical application, as compared with 10 weeks for wild-type mice (top graph in Fig. 1B). The number of papillomas was also significantly greater in K14-*Angptl2* Tg (bottom graph in Fig. 1B). At 20 weeks after beginning of chemical treatment, K14-*Angptl2* Tg exhibited an average of 29.8 papillomas per mouse, compared with 8.1 in wild-type mice ($P < 0.001$). When only large papillomas (diameter >3 mm) were evaluated, K14-*Angptl2* Tg developed papillomas 5 weeks earlier than did wild-type mice (top graph in Fig. 1C), and the average number of large papillomas was increased 3.7-fold in K14-*Angptl2* Tg (bottom graph in Fig. 1C). Notably, there was no difference in the ratio of large papillomas to the total number between them (Fig. 1D). By 25 weeks after initiation of treatment, more than 80% of K14-*Angptl2* Tg had developed malignant SCC, whereas only 50% of wild-type mice developed malignant SCC by this time point (top graph in Fig. 1E). The average number of SCC tumors was increased 5.44-fold in K14-*Angptl2* Tg (bottom graph in Fig. 1E). As observed in Fig. 1F, the formation of SCC tumors was enhanced in K14-*Angptl2* Tg. Histologic analysis confirmed that most large tumors were SCCs (Supplementary Fig. S7A and B). SCCs in K14-*Angptl2* Tg were poorly differentiated and had lost their epithelial properties by acquisition of mesenchymal morphology. The malignant conversion rate, defined as the ratio of SCCs to the number of large papillomas, in K14-*Angptl2* Tg was greater than that calculated for wild-type mice (Fig. 1G). Thus, Angptl2 overexpression enhances susceptibility to "preneoplastic change" and "malignant conversion" in this model. Furthermore, we found that expression levels of the inflammatory marker *IL-1β* in both skin tissues after chemical treatment (Supplementary Fig. S8A) and papilloma (Supplementary Fig. S9A) of K14-*Angptl2* Tg were significantly increased compared with wild-type mice, suggesting that Angptl2-associated inflammation may promote susceptibility to "preneoplastic change" and "malignant conversion" in this model.

Angptl2 activation in tumor cells promotes metastasis to distant organs and lymph nodes

Although lung metastasis was detected in both K14-*Angptl2* Tg and wild-type mice, its frequency was significantly increased in K14-*Angptl2* Tg (Fig. 2A). The severity of metastasis, as indicated by the number and area of metastatic lung tumor sites in the H&E stained section, was greater in K14-*Angptl2* Tg compared with wild-type mice (Fig. 2B and C). Notably, 66.7% of K14-*Angptl2* Tg showed metastasis to lung and more than 30% showed metastasis to both spleen and liver (Supplementary Fig. S10). In contrast, 17.6% of wild-type mice showed metastasis only to lung but not to spleen or liver. K14-*Angptl2* Tg also showed increased frequency of metastasis to lymph nodes (Fig. 2D) and exhibited significantly enlarged lymph nodes compared with wild-type mice (Fig. 2E and F). Histologic analysis confirmed that enlarged lymph nodes were due to tumor cell metastasis rather than to inflammatory swelling (Fig. 2E). Finally, when we compared survival periods after development of malignant SCC, K14-*Angptl2* Tg showed significantly shortened survival compared with wild-type mice (Fig. 2G). Expression levels of the inflammatory markers *IL-6* and *IL-1β* in SCC of K14-*Angptl2* Tg were also significantly increased compared with wild-type mice (Supplementary Fig. S11A), suggesting that Angptl2-associated inflammation might be attributable to increased tumor metastasis in K14-*Angptl2* Tg.

Suppressed carcinogenesis in skin tissues of *Angptl2* knockout mice

On the basis of our observation that Angptl2 overexpression enhances susceptibility to carcinogenesis and increases tumor metastasis, we asked whether *Angptl2* deletion altered these pathologies. Therefore, we subjected *Angptl2* KO and wild-type mice to the skin carcinogenesis regimen. We observed no papillomas or carcinoma in wild type or *Angptl2* KO treated with DMBA alone or PMA alone (data not shown). When mice were treated with both chemicals, papilloma formation in *Angptl2* KO was suppressed compared with wild-type mice (Fig. 3A). The average latency period for formation of skin papillomas in *Angptl2* KO was 15 weeks after chemical application, compared with 10 weeks in wild-type mice (top graph in Fig. 3B). At 20 weeks after treatment, *Angptl2* KO exhibited an average of 2.6 papillomas per mouse compared with 7.7 in wild-type mice (bottom graph in Fig. 3B). When only large papillomas were evaluated, *Angptl2* KO developed large papillomas 4 weeks later than did wild-type mice (top graph in Fig. 3C), and the average number of large papillomas was also decreased 0.25-fold in *Angptl2* KO (bottom graph in Fig. 3C). Notably, there was no difference in the ratio of large papillomas to the total number between them (Fig. 3D). By 25 weeks after treatment, about 50% of wild-type mice had developed malignant SCC, whereas only 10% of *Angptl2* KO developed malignant SCC by this time point (top graph in Fig. 3E). At 25 weeks after treatment, the average number of SCC lesions was decreased 0.14-fold in *Angptl2* KO compared with wild-type mice (bottom graph in Fig. 3E). As shown in Fig. 3F, SCC development was significantly attenuated in *Angptl2* KO. In contrast to SCCs in wild-type mice, SCCs in *Angptl2* KO were histologically well-differentiated tumors and tended to be organized in epithelial structures (Supplementary Fig. S7C and D). The malignant conversion rate, defined as a ratio of SCC lesions to the number of large papillomas, was lower in *Angptl2* KO than in wild-type mice (Fig. 3G). By contrast to findings in K14-*Angptl2* Tg, expression levels of inflammatory markers in skin tissues before (Supplementary Fig. S5B) and after (Supplementary Fig. S8B) chemical treatment and in papillomas (Supplementary Fig. S9B) of *Angptl2* KO were decreased compared with wild-type mice. Thus the absence of Angptl2-induced inflammation may underlie attenuation of "preneoplastic change" and "malignant conversion" in carcinogenesis in *Angptl2* KO.

Published OnlineFirst October 31, 2011; DOI:10.1158/0008-5472.CAN-11-1758

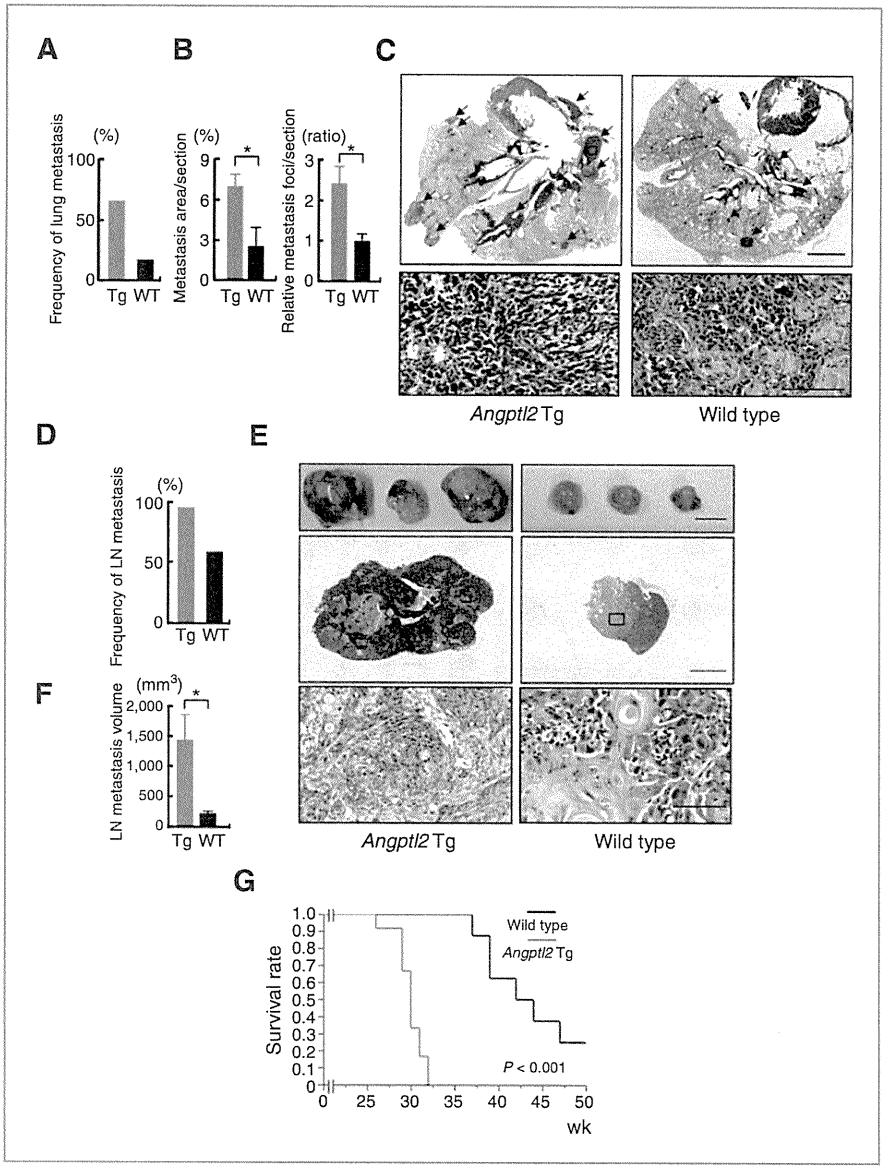

Figure 2. K14-*Angptl2* transgenic mice show enhanced metastasis and shortened survival. A, comparison of frequency of lung metastasis events between K14-*Angptl2* Tg ($n = 21$) and wild-type mice ($n = 17$). B, quantitative comparison of lung metastasis in K14-*Angptl2* Tg ($n = 6$) and wild-type mice ($n = 5$) on the basis of the area of tumor cells per area of a lung section (left) and the relative number of metastatic foci per a lung section (right, wild-type data set at 1). C, H&E-stained lung tissues of K14-*Angptl2* Tg and wild-type mice. Arrows indicate masses of metastatic tumor cells. Bottom panels are magnifications of squares in top panels. Scale bar, 2.5 mm (top), 100 μm (bottom). D, comparison of frequency of metastasis to lymph nodes (LN) between K14-Angptl2 Tg ($n = 21$) and wild-type mice ($n = 17$). E, photograph of gross appearance (top) and H&E staining (middle and bottom) of lymph node from K14-*Angptl2* Tg and wild-type mice. Bottom panels are magnifications of squares in middle panels. Scale bar, 10 mm (top), 4 mm (middle), 100 μm (bottom). F, comparison of lymph node volume in K14-*Angptl2* Tg ($n = 6$) and wild-type mice ($n = 6$). G, Kaplan–Meier survival curves after initiation of chemical application of K14-*Angptl2* Tg ($n = 12$) and wild-type mice ($n = 8$; $P < 0.001$ by log-rank test). Data shown in B and F represent means ± SEM. WT, wild type. *, $P < 0.05$.

Angptl2 knockout mice show decreased lung and lymph node metastasis

At 8 weeks after detection of the first SCC, 16.7% of wild-type mice showed metastasis to lung, whereas no metastases were seen in *Angptl2* KO (Fig. 4A). Metastatic colonies of tumor cells were detected at multiple sites within the lung of wild-type mice, whereas none were seen in *Angptl2* KO (Fig. 4B). Although metastasis to lymph nodes was detected in both genotypes, the frequency of metastasis was significantly lower in *Angptl2* KO compared with wild-type mice (Fig. 4C). The severity of metastasis, as estimated by the size of metastatic lymph node sites, in *Angptl2* KO was also significantly decreased relative to that seen in wild-type mice (Fig. 4D and E). Finally, survival of *Angptl2* KO was significantly prolonged compared with that of wild-type mice (Fig. 4F). Expression of *IL-6* and *IL-1β* in SCC of *Angptl2* KO was also significantly decreased compared with that seen in wild-type mice (Supplementary Fig. S11B), suggesting that decreased tumor metastasis in *Angptl2* KO may be due to the absence of Angptl2-induced inflammation in SCC.

Angptl2 derived from SCC contributes to tumor angiogenesis and lymphangiogenesis

Tumor angiogenesis and lymphangiogenesis are essential for tumor growth and metastasis. Because we previously reported that Angptl2 activates endothelial cell motility (9), we asked whether the extent of SCC tumor vasculature induced by chemical carcinogenesis differed between K14-*Angptl2* Tg

Published OnlineFirst October 31, 2011; DOI:10.1158/0008-5472.CAN-11-1758

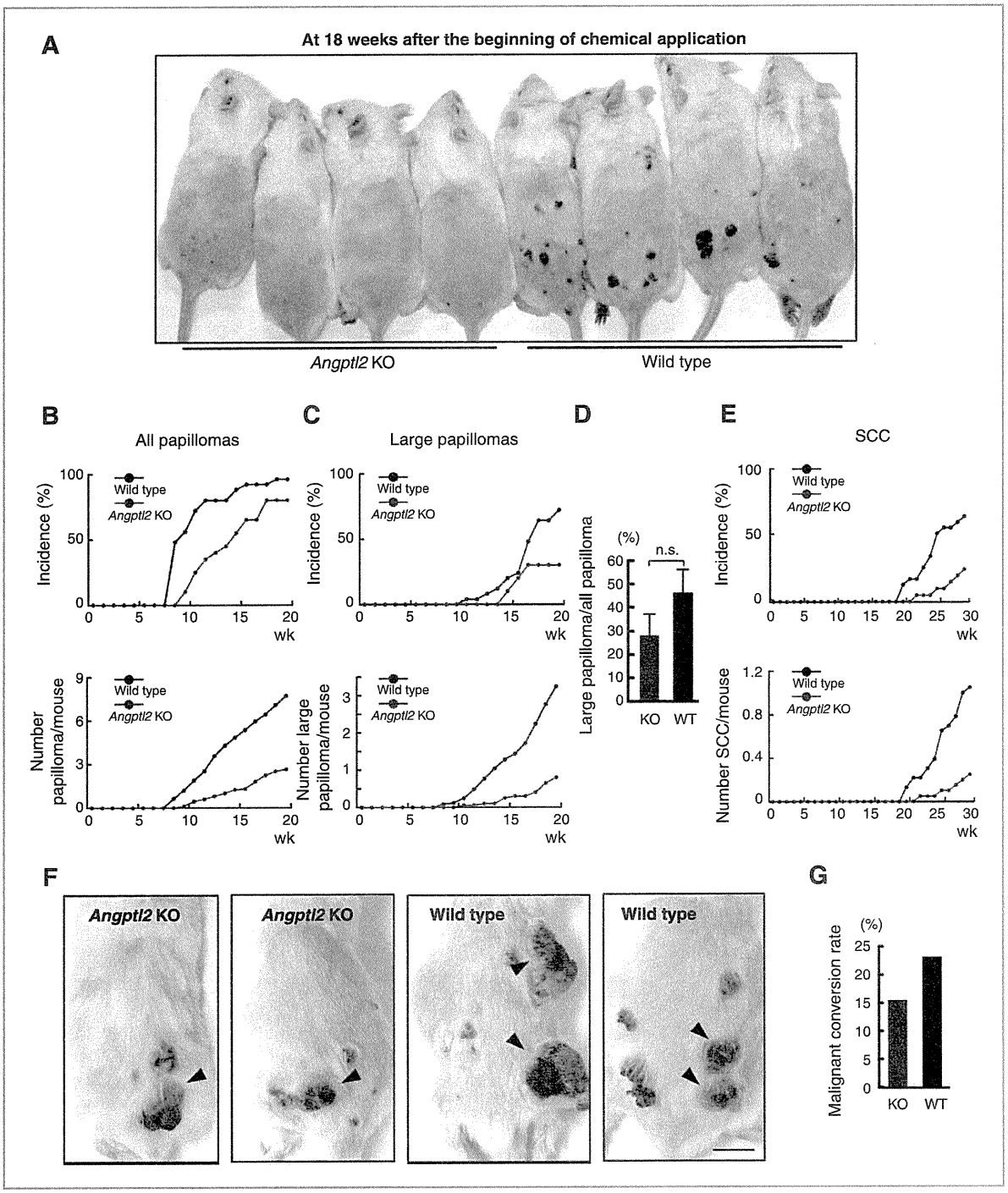

Figure 3. *Angptl2* knockout mice show suppressed and decreased skin carcinogenesis. A, photograph of skin of *Angptl2* KO (left) and wild-type mice (right) 18 weeks after initiation of chemical application. B and C, the incidence (top graphs) and number (bottom graphs) of all detectable (B) and large papillomas (C) on *Angptl2* KO ($n = 20$; blue circles) and wild-type mice ($n = 25$; black circles) after initiation of chemical application. $P < 0.01$ from weeks 10 to 20 (bottom graph in B), $P < 0.05$ from weeks 14 to 16, $P < 0.01$ from weeks 17 to 20 (bottom graph in C). D, proportion of large compared with detectable papillomas in *Angptl2* KO versus wild-type mice. Data represent means ± SEM. n.s., not significant. E, decreased incidence of SCC (top graph) and number of SCC per mouse (bottom graph, $P < 0.05$ at weeks 24, $P < 0.01$ after weeks 25) in *Angptl2* KO ($n = 33$; blue circles) compared with wild-type mice ($n = 34$; black circles). F, photograph of SCC on *Angptl2* KO (left 2 panels) and wild-type mice (right 2 panels) 8 weeks after first SCC diagnosis. Arrowheads indicate SCC. Scale bars, 10 mm. G, malignant conversion rate of large papillomas to SCC in *Angptl2* KO and wild-type mice. WT, wild type.

Published OnlineFirst October 31, 2011; DOI:10.1158/0008-5472.CAN-11-1758

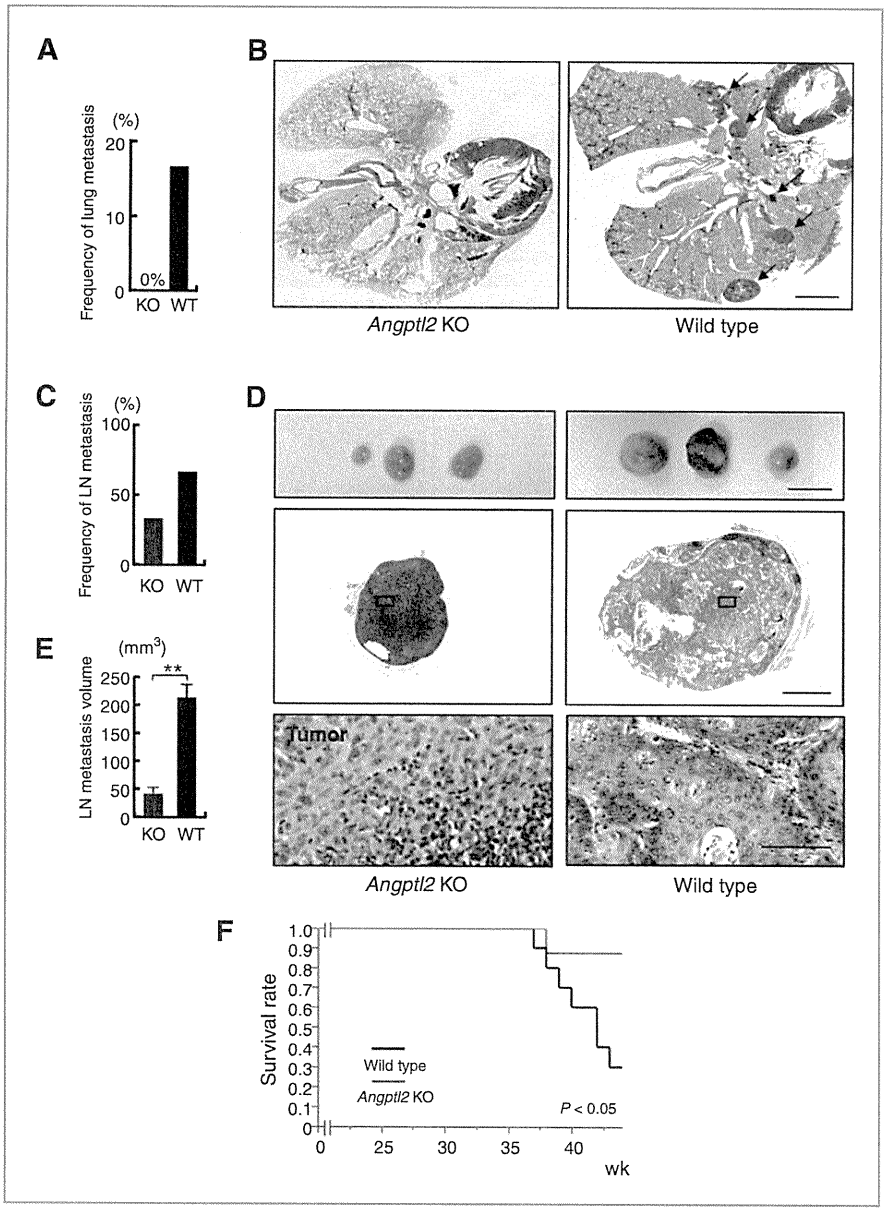

Figure 4. *Angptl2* knockout mice show decreased metastasis and prolonged survival. A, frequency of metastasis to distant secondary organs in *Angptl2* KO ($n = 21$) versus wild-type mice ($n = 17$). B, H&E-stained lung tissues of *Angptl2* KO (left) and wild-type mice (right). Arrows indicate metastatic foci in wild-type. Scale bar, 2.5 mm. C, frequency of metastasis to lymph nodes (LN) between *Angptl2* KO ($n = 21$) and wild-type mice ($n = 17$). D, gross appearance (top) and H&E staining (middle and bottom) of lymph nodes of *Angptl2* KO and wild-type mice. Bottom panels are magnifications of squares in middle panels. Scale bar, 10 mm (top), 2 mm (middle), 100 μm (bottom). E, comparison of lymph node volume in K14-*Angptl2* Tg ($n = 6$) and wild-type mice ($n = 6$). Data represent means ± SEM. **, $P < 0.01$. F, Kaplan–Meier survival curves after initiating chemical application between *Angptl2* KO ($n = 8$) and wild-type mice ($n = 10$; $P < 0.05$ by log-rank test). WT, wild type.

and wild-type mice. We found that blood vessels invading cancer tissues from surrounding tissues in K14-*Angptl2* Tg were more prominent than those in wild-type mice (Fig. 5A). Quantitative analysis revealed that the area occupied by both CD31-positive blood vessels and LYVE-1–positive lymphatic vessels was significantly increased in cancer tissues of K14-*Angptl2* Tg compared with wild-type mice (Supplementary Fig. S12A and B), suggesting that Angptl2 enhances tumor vasculature. In contrast, the number of blood vessels invading tumor sites from surrounding tissues in *Angptl2* KO seemed to be decreased compared with wild-type mice (Fig. 5B). The area occupied by both blood vessels and lymphatic vessels was quantitatively decreased in tumor tissues of *Angptl2* KO versus wild-type mice (Supplementary Fig. S12C and D). The extent of Evans blue dye leakage from SCC tumors was markedly attenuated in *Angptl2* KO compared with wild-type mice (Supplementary Fig. S13A), a finding confirmed quantitatively (Supplementary Fig. S13B).

The epithelial-to-mesenchymal transition correlates with Angptl2 expression levels

H&E staining of SCC tumor cells in K14-*Angptl2* Tg revealed neither an ordered structure nor tight cell–cell adhesion compared with wild-type mice (Supplementary Fig. S14A).

Published OnlineFirst October 31, 2011; DOI:10.1158/0008-5472.CAN-11-1758

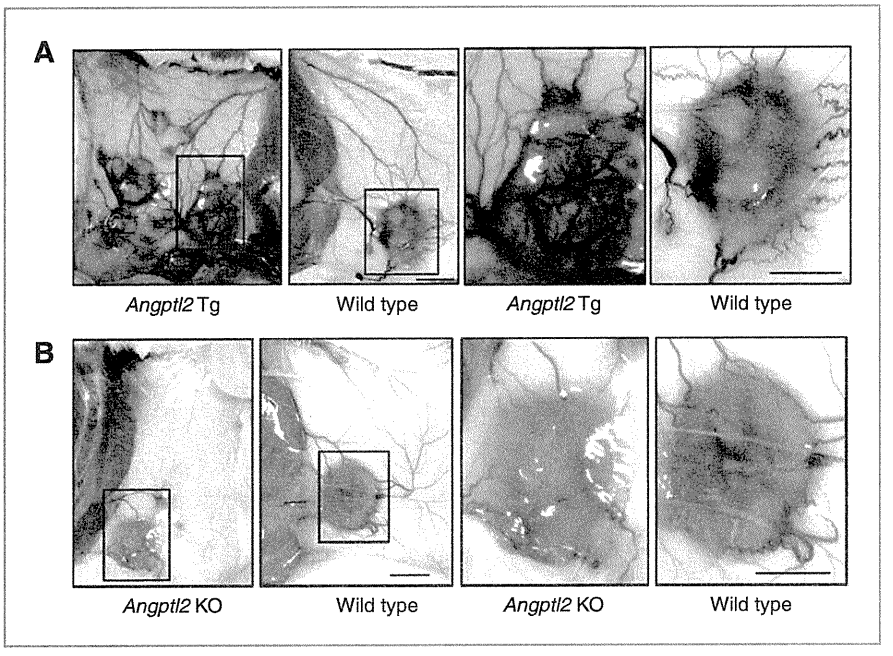

Figure 5. Angptl2 derived from cancer cells contributes to tumor angiogenesis and lymphangiogenesis. A, photograph of vasculature in primary tumors induced by chemical skin carcinogenesis of K14-*Angptl2* Tg and wild-type mice. Right 2 panels are magnifications of squares in left panels, respectively. Scale bar, 10 mm (left), 10 mm (right). B, photograph of vasculature of primary tumors induced by chemical skin carcinogenesis of *Angptl2* KO and wild-type mice. Right 2 panels are magnifications of squares in left panels, respectively. Scale bar, 10 mm (left), 10 mm (right).

Instead, tumor cells showed an irregular structure, appeared more elongated, and were not uniform in composition or density. Because a critical event in tumor metastasis is a decrease in cancer cell adhesion through acquisition of mesenchymal phenotypes and invasive properties, we asked whether Angptl2 increases the epithelial-to-mesenchymal transition (EMT) in SCC. Relative to wild-type mice, increased *N-cadherin*, *Slug*, and *Snail* mRNA, as mesenchymal markers and decreased *E-cadherin* mRNA, as an epithelial indicator were observed in SCC of K14-*Angptl2* Tg (Supplementary Fig. S15A). Immunohistochemical analysis also revealed increased N-cadherin expression, decreased E-cadherin expression, and increased nuclear levels of Slug and Snail in SCC of K14-*Angptl2* Tg compared with wild-type mice (Fig. 6A), suggesting that constitutive activation of Angptl2 signaling may underlie EMT. Conversely, H&E staining showed that SCC tumor cells in *Angptl2* KO formed a sheet (Supplementary Fig. S14B) and abutted each other in a uniform array. Furthermore, decreased *N-cadherin*, *Slug*, and *Snail* mRNA and increased *E-cadherin* mRNA were observed in SCC of *Angptl2* KO compared with wild-type mice (Supplementary Fig. S15B). Immunohistochemical analysis also revealed decreased E-cadherin expression and increased nuclear Slug and Snail in SCC from wild-type mice, whereas SCC of *Angptl2* KO exhibited primarily epithelial phenotypes and showed little nuclear translocation of Slug or Snail (Fig. 6B). TGF-β/Smad signaling plays a pivotal role in promoting EMT (21–23). To investigate mechanisms underlying activation of EMT seen in the presence of Angptl2 overexpression, we analyzed activation of this pathway. We observed increased expression of *TGF-β1*, *TGF-β2*, *TGF-βR1*, and *TGF-βR2* mRNAs in SCC of K14-*Angptl2* Tg compared with wild-type mice (Supplementary Fig. S15C). Conversely, we observed decreased relative expression of those genes in SCC of *Angptl2* KO mice (Supplementary Fig. S15D). In addition, phosphorylation of Smad2, a TGF-β effector, was significantly decreased in SCC of *Angptl2* KO, whereas Smad2 phosphorylation was significantly increased in SCC of K14-*Angptl2* Tg compared with controls (Fig. 6C). These findings suggested that Angptl2 promotes EMT via activating the TGF-β–Smad pathway.

Discussion

Here, we found that skin tissues expressing abundant Angptl2 exhibit high carcinogenic potential in a chemically induced skin SCC mouse model through increased susceptibility to both "preneoplastic change" and "malignant conversion", although abundant Angptl2 expression in skin tissues could not cause SCC. Furthermore, Angptl2 derived from SCC increased cancer cell metastasis to both distant secondary organs and lymph nodes, presumably, by promoting both EMT in cancer cells and tumor angiogenesis and lymphangiogenesis.

The initiating oncogenic mutation within a normal cell is essential for "preneoplastic change." It is also important that cells harboring that mutation acquire the proliferation and survival capacity to allow accumulation of additional mutations (24–26). When an oncogenic mutation occurs within a normal cell, DNA repair mechanisms often avert carcinogenesis. However, increased accumulation of reactive oxygen species (ROS) and reactive nitrogen intermediates because of chronic inflammation can inactivate DNA repair enzymes (27). In this regard, both chronic inflammatory status and ROS levels in mouse skin tissues are positively correlated with Angptl2

Published OnlineFirst October 31, 2011; DOI:10.1158/0008-5472.CAN-11-1758

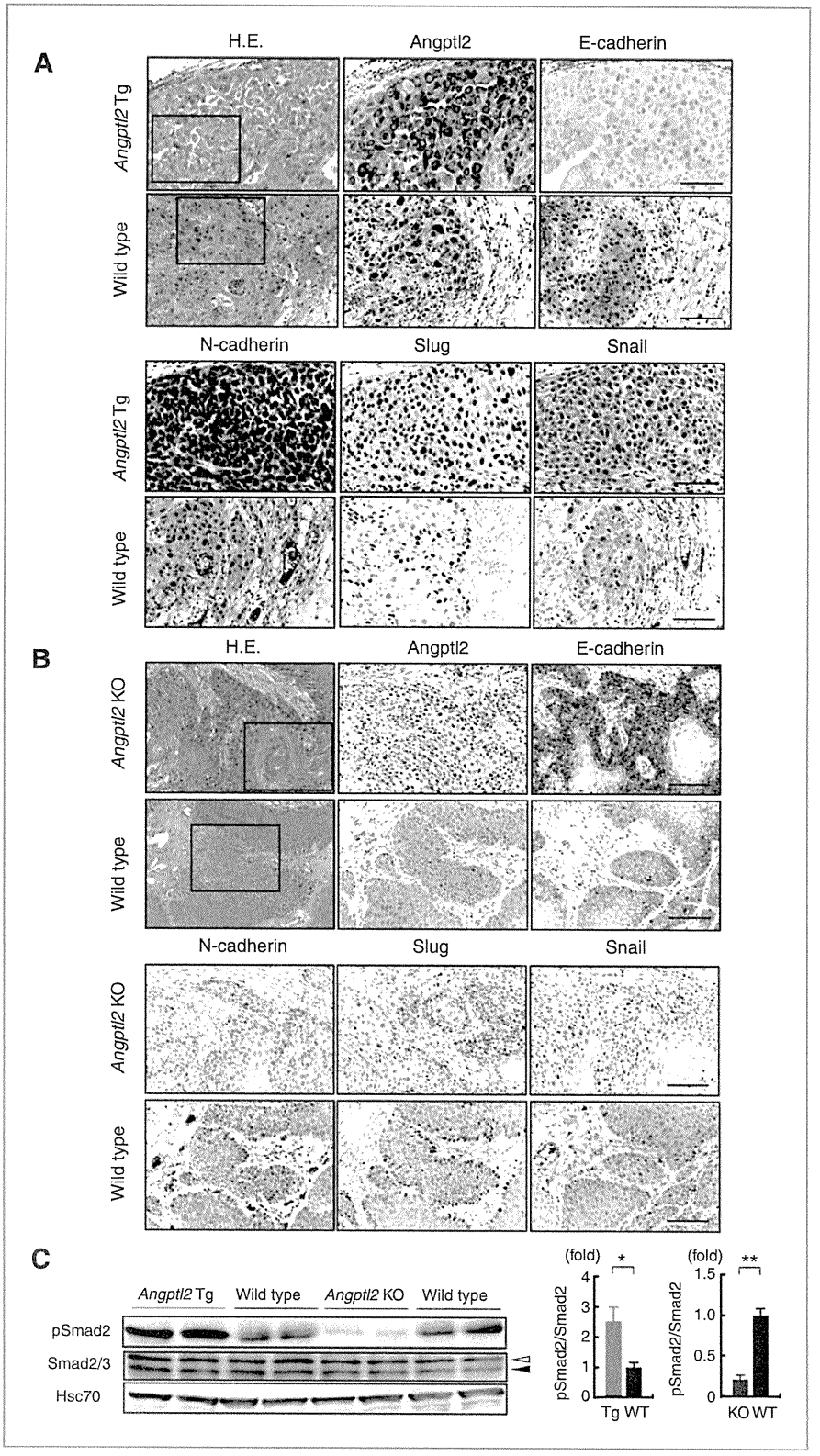

Figure 6. Angptl2 expression levels are correlated with the epithelial-to-mesenchymal transition. A and B, H&E staining and immunohistochemical staining for Angptl2, E-cadherin, N-cadherin, Slug, and Snail in primary tumor tissue of K14-*Angptl2* Tg and wild-type mice (A) and *Angptl2* KO and wild-type mice (B). C, left, Western blotting analysis of phosphorylated Smad2, total Smad2/3, and Hsc70 in primary tumor tissue. Open and closed arrowheads indicate Smad2 and Smad3, respectively. Right, quantitative analysis of Western blotting analysis ($n = 3$). Scale bars, 100 μm. Data are expressed as means ± SEM. *, $P < 0.05$; **, $P < 0.01$ compared with wild-type mice.

Published OnlineFirst October 31, 2011; DOI:10.1158/0008-5472.CAN-11-1758

expression levels (Supplementary Fig. S16), suggesting that Angptl2-associated inflammation creates a microenvironment conducive to DNA damage and genomic instability. Normal skin stem cells or transit amplifying cells are more susceptible to mutation than are differentiated cells (2). An inflammatory microenvironment reportedly increases the number of stem cells and transit amplifying cells (27), suggesting that Angptl2-associated inflammatory changes in skin tissues might increase these stem cell populations. However, we observed no difference in the number of normal skin stem cells as estimated by a long-time pulse of bromodeoxyuridine incorporation experiment (28) among *Angptl2* KO, K14-*Angptl2* Tg, and their respective wild-type littermates (data not shown). Taken together, we propose that Angptl2 increased susceptibility to both "preneoplastic change" and "malignant conversion" is more likely due to differences in the microenvironment conducive to maintenance of oncogenic DNA mutations and accumulation of additional mutations.

Although we found no papillomas or carcinoma at any time point in either K14-*Angptl2* Tg, *Angptl2* KO, or wild-type mice treated with PMA alone (data not shown), treatment with PMA only did induce Angptl2 expression in wild-type mice (Supplementary Fig. S6). In analysis of human subjects, Angptl2 expression in skin tissues exposed to sunlight was increased compared with tissues not exposed to sun (Supplementary Fig. S17), suggesting Angptl2 induction in skin cells by sunburn might increase cancer susceptibility. This finding is consistent with the well-established idea that sunburn increases the risk of skin carcinogenesis because of DNA damage and inflammation (19, 29). Most solid malignancies appear in older subjects, and aging or cell senescence is postulated to function as cancer promoters that act through inflammatory mechanisms. Accordingly, Angptl2 expression in regions not exposed to sun was elevated in parallel with aging in human subjects (Supplementary Fig. S18). Sunburn- or aging-induced Angptl2 and its related chronic inflammation in skin tissue might increase susceptibility to skin carcinogenesis.

Angptl2 is reportedly a putative tumor suppressor in ovarian cancer (15). In that report, lack of Angptl2 immunoreactivity in tumor cells was associated with poorer overall survival in stage I and II disease, whereas Angptl2 positivity was significantly associated with a poorer survival in stage III and IV disease. The latter findings are consistent with our own, suggesting that Angptl2 is critical for tumor progression and metastasis. Here, we did not observe a tumor suppressor function for Angptl2 in skin cells. Whether Angptl2 function differs in various tumor cell types remains to be determined.

This study shows that Angptl2 expression increases carcinogenesis through enhanced susceptibility to both "preneoplastic change" and "malignant conversion." Chronic inflammatory status during carcinogenesis was markedly different among K14-*Angptl2* Tg, *Angptl2* KO, and wild-type mice, and it depended on Angptl2 expression levels. This suggested that Angptl2-associated chronic inflammation is important for cancer susceptibility. Angptl2 derived from tumor cells significantly increased distant secondary organ metastasis and lymph node metastasis through acquisition of EMT-related invasive properties, in addition to promoting tumor angiogenesis and lymphangiogenesis (Supplementary Fig. S19). Overall, our findings suggest that Angptl2 represents a new target for prevention of these activities in preneoplastic lesions and cancers that express Angptl2.

Disclosure of Potential Conflicts of Interest

No potential conflicts of interest were disclosed.

Acknowledgments

The authors thank Mss. S. Iwaki, O. Takahashi, and M. Nakata for technical assistance.

Grant Support

This work was supported by grants-in-aid for Scientific Research on Priority Areas from the Ministry of Education, Culture, Sports, Science and Technology of Japan, by the Japan Society for the Promotion of Science (JSPS) through its Funding Program for Next Generation World-Leading Researchers (NEXT Program), and by grants from the Takeda Science Foundation, the Mitsubishi Foundation, and the Tokyo Biochemical Research Foundation.

The costs of publication of this article were defrayed in part by the payment of page charges. This article must therefore be hereby marked *advertisement* in accordance with 18 U.S.C. Section 1734 solely to indicate this fact.

Received May 26, 2011; revised October 10, 2011; accepted October 24, 2011; published OnlineFirst October 31, 2011.

References

1. Chiang AC, Massague J. Molecular basis of metastasis. N Engl J Med 2008;359:2814–23.
2. Grivennikov SI, Greten FR, Karin M. Immunity, inflammation, and cancer. Cell 2010;140:883–99.
3. de Martel C, Franceschi S. Infections and cancer: established associations and new hypotheses. Crit Rev Oncol Hematol 2009;70:183–94.
4. Takahashi H, Takahashi I, Honma M, Ishida-Yamamoto A, Iizuka H. Prevalence of metabolic syndrome in Japanese psoriasis patients. J Dermatol Sci 2010;57:143–4.
5. Dostert C, Petrilli V, Van Bruggen R, Steele C, Mossman BT, Tschopp J. Innate immune activation through Nalp3 inflammasome sensing of asbestos and silica. Science 2008;320:674–7.
6. Kant P, Hull MA. Excess body weight and obesity-the link with gastrointestinal and hepatobiliary cancer. Nat Rev Gastroenterol Hepatol 2011;8:224–38.
7. Calle EE. Obesity and cancer. BMJ 2007;335:1107–8.
8. Park EJ, Lee JH, Yu GY, He G, Ali SR, Holzer RG, et al. Dietary and genetic obesity promote liver inflammation and tumorigenesis by enhancing IL-6 and TNF expression. Cell 2010;140:197–208.
9. Tabata M, Kadomatsu T, Fukuhara S, Miyata K, Ito Y, Endo M, et al. Angiopoietin-like protein 2 promotes chronic adipose tissue inflammation and obesity-related systemic insulin resistance. Cell Metab 2009;10:178–88.
10. Bi M, Naczki C, Koritzinsky M, Fels D, Blais J, Hu N, et al. ER stress-regulated translation increases tolerance to extreme hypoxia and promotes tumor growth. EMBO J 2005;24:3470–81.
11. Crawford Y, Kasman I, Yu L, Zhong C, Wu X, Modrusan Z, et al. PDGF-C mediates the angiogenic and tumorigenic properties of fibroblasts associated with tumors refractory to anti-VEGF treatment. Cancer Cell 2009;15:21–34.
12. Okada T, Tsukano H, Endo M, Tabata M, Miyata K, Kadomatsu T, et al. Synoviocyte-derived angiopoietin-like protein 2 contributes to

Published OnlineFirst October 31, 2011; DOI:10.1158/0008-5472.CAN-11-1758

synovial chronic inflammation in rheumatoid arthritis. Am J Pathol 2010;176:2309–19.
13. Avraamides CJ, Garmy-Susini B, Varner JA. Integrins in angiogenesis and lymphangiogenesis. Nat Rev Cancer 2008;8:604–17.
14. Desgrosellier JS, Cheresh DA. Integrins in cancer: biological implications and therapeutic opportunities. Nat Rev Cancer 2010;10:9–22.
15. Kikuchi R, Tsuda H, Kozaki K, Kanai Y, Kasamatsu T, Sengoku K, et al. Frequent inactivation of a putative tumor suppressor, angiopoietin-like protein 2, in ovarian cancer. Cancer Res 2008;68:5067–75.
16. Yuspa SH, Døugosz AA, Cheng CK, Denning MF, Tennenbaum T, Glick AB, et al. Role of oncogenes and tumor suppressor genes in multistage carcinogenesis. J Invest Dermatol. 1994;103:90S–5S.
17. Hawighorst T, Velasco P, Streit M, Hong YK, Kyriakides TR, Brown LF, et al. Thrombospondin-2 plays a protective role in multistep carcinogenesis: a novel host anti-tumor defense mechanism. EMBO J 2001;20:2631–40.
18. Hawighorst T, Oura H, Streit M, Janes L, Nguyen L, Brown LF, et al. Thrombospondin-1 selectively inhibits early-stage carcinogenesis and angiogenesis but not tumor lymphangiogenesis and lymphatic metastasis in transgenic mice. Oncogene 2002;21:7945–56.
19. Yuspa SH. The pathogenesis of squamous cell cancer: lessons learned from studies of skin carcinogenesis. J Dermatol Sci 1998;17:1–7.
20. Yuspa SH. Overview of carcinogenesis: past, present and future. Carcinogenesis 2000;21:341–4.
21. Ikushima H, Miyazono K. TGF-β signalling: a complex web in cancer progression. Nat Rev Cancer 2010;10:415–24.
22. Massague J. TGF-β in Cancer. Cell 2008;134:215–30.
23. Bierie B, Moses HL. Tumour microenvironment: TGF-β: the molecular Jekyll and Hyde of cancer. Nat Rev Cancer 2006;6:506–20.
24. Knudson AG. Two genetic hits (more or less) to cancer. Nat Rev Cancer 2001;1:157–62.
25. Hanahan D, Weinberg RA. Hallmarks of cancer: the next generation. Cell 2011;144:646–74.
26. Fearon ER, Vogelstein B. A genetic model for colorectal tumorigenesis. Cell 1990;61:759–67.
27. Colotta F, Allavena P, Sica A, Garlanda C, Mantovani A. Cancer-related inflammation, the seventh hallmark of cancer: links to genetic instability. Carcinogenesis 2009;30:1073–81.
28. Cotsarelis G, Sun TT, Lavker RM. Label-retaining cells reside in the bulge area of pilosebaceous unit: implications for follicular stem cells, hair cycle, and skin carcinogenesis. Cell 1990;61:1329–37.
29. Alam M, Ratner D. Cutaneous squamous-cell carcinoma. N Engl J Med 2001;344:975–83.

Lipoxygenase mediates invasion of intrametastatic lymphatic vessels and propagates lymph node metastasis of human mammary carcinoma xenografts in mouse

Dontscho Kerjaschki,[1,2] Zsuzsanna Bago-Horvath,[1,2,3] Margaretha Rudas,[1,2,3] Veronika Sexl,[4] Christine Schneckenleithner,[4] Susanne Wolbank,[5] Gregor Bartel,[1] Sigurd Krieger,[1] Romana Kalt,[1] Brigitte Hantusch,[1,2] Thomas Keller,[1] Katalin Nagy-Bojarszky,[1] Nicole Huttary,[1] Ingrid Raab,[1] Karin Lackner,[1] Katharina Krautgasser,[1] Helga Schachner,[1] Klaus Kaserer,[1] Sandra Rezar,[1] Sybille Madlener,[1] Caroline Vonach,[1] Agnes Davidovits,[1] Hitonari Nosaka,[1] Monika Hämmerle,[1] Katharina Viola,[1] Helmut Dolznig,[1] Martin Schreiber,[6] Alexander Nader,[7] Wolfgang Mikulits,[2,8] Michael Gnant,[2,3,9] Satoshi Hirakawa,[10] Michael Detmar,[11] Kari Alitalo,[12] Sebastian Nijman,[13] Felix Offner,[14] Thorsten J. Maier,[15] Dieter Steinhilber,[15] and Georg Krupitza[1,2]

[1]Clinical Institute of Pathology, [2]Comprehensive Cancer Center, [3]Austrian Breast and Colorectal Cancer Study Group (ABCSG), and [4]Institute of Pharmacology, Medical University of Vienna, Vienna, Austria. [5]Ludwig Boltzmann Institute for Experimental and Clinical Traumatology, Vienna, Austria. [6]Department of Gynaecology, Medical University of Vienna, Vienna, Austria. [7]Pathology Institute, Hanusch Hospital, Vienna, Austria. [8]Institute of Cancer Research and [9]Department of Surgery, Medical University of Vienna, Vienna, Austria. [10]Department of Dermatology, Ehime University Graduate School of Medicine, Ehime, Japan. [11]Department of Pharmacogenomics, Swiss Federal Institute of Technology ETH-Zurich, Zurich, Switzerland. [12]Molecular/Cancer Biology Laboratory, Biomedicum Helsinki, University of Helsinki, Helsinki, Finland. [13]Ce-M-M-Research Center for Molecular Medicine of the Austrian Academy of Sciences, Vienna, Austria. [14]Institute for Pathology, LKH Feldkirch, Austria. [15]Institute of Pharmaceutical Chemistry/ZAFES, Frankfurt/Main, Germany.

In individuals with mammary carcinoma, the most relevant prognostic predictor of distant organ metastasis and clinical outcome is the status of axillary lymph node metastasis. Metastases form initially in axillary sentinel lymph nodes and progress via connecting lymphatic vessels into postsentinel lymph nodes. However, the mechanisms of consecutive lymph node colonization are unknown. Through the analysis of human mammary carcinomas and their matching axillary lymph nodes, we show here that intrametastatic lymphatic vessels and bulk tumor cell invasion into these vessels highly correlate with formation of postsentinel metastasis. In an in vitro model of tumor bulk invasion, human mammary carcinoma cells caused circular defects in lymphatic endothelial monolayers. These circular defects were highly reminiscent of defects of the lymphovascular walls at sites of tumor invasion in vivo and were primarily generated by the tumor-derived arachidonic acid metabolite 12S-HETE following 15-lipoxygenase-1 (ALOX15) catalysis. Accordingly, pharmacological inhibition and shRNA knockdown of ALOX15 each repressed formation of circular defects in vitro. Importantly, ALOX15 knockdown antagonized formation of lymph node metastasis in xenografted tumors. Furthermore, expression of lipoxygenase in human sentinel lymph node metastases correlated inversely with metastasis-free survival. These results provide evidence that lipoxygenase serves as a mediator of tumor cell invasion into lymphatic vessels and formation of lymph node metastasis in ductal mammary carcinomas.

Introduction

A tumor's metastatic potential is determined by complex and specific genetic gains and/or losses of function that enable tumor cells to emigrate from their primary site to access the blood or lymphatic vasculature and to form premetastatic niches in target organs that provide the essential "soil" for "seeding" of incoming tumor cells (1). Despite the obvious clinical relevance of these events, relatively little is currently known about the underlying mechanisms. For example, only some aspects of niche formation in distant organs have been identified; these include local accumulation of bone marrow–derived cells, fibronectin deposition (2), and interactions between tumor cells and thrombocytes (3).

Whether tumors metastasize initially into lymph nodes or are distributed by hematogenous dissemination into distant organs remains a matter for debate, and there is experimental evidence for each hypothesis (4–6). One view holds that metastatic tumor cells colonize distant organs via the blood stream either from lymph nodes ("metastasis from metastasis") (7) or by cross seeding from the primary tumor by recirculation (8). Alternatively, clonogenic tumor cells, presumably with stem cell–like characteristics, could disseminate simultaneously at an early time point from primary tumors into both the blood and lymphatic vasculature and then develop metastases asynchronously in both compartments (9). Although currently evidence is accumulating in favor of the latter hypothesis (5), it falls short of explaining why the number of regional lymph nodes affected by metastases most accurately predicts the general extent of metastatic spreading and overall clinical outcome, for

Conflict of interest: The authors have declared that no conflict of interest exists.
Citation for this article: *J Clin Invest.* 2011;121(5):2000–2012. doi:10.1172/JCI44751.

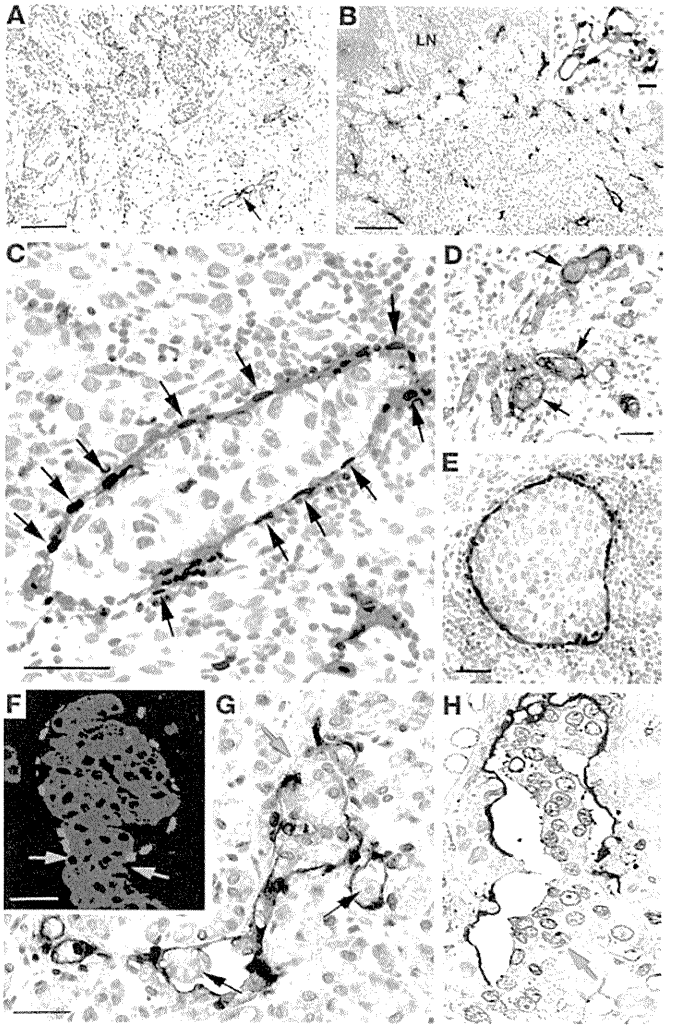

Figure 1
Intrametastatic lymphangiogenesis and tumor cell invasion into lymphatic vessels in sentinel lymph nodes of human ductal mammary carcinomas with postsentinel metastasis. Lymphatic endothelial cells are localized by double labeling for podoplanin (red) and PROX1 (black) in **A**–**C** and **E**. (**A**) In a primary ductal carcinoma, lymphatic vessels are localized in the peritumoral stroma (arrow). The tumor border is marked by a green line. (**B**) Sentinel lymph node metastasis of the same carcinoma as in part **A**, with dense intrametastatic lymphatic vascularization. LN, residual lymph node parenchyma. Insert, FLT4 (red) in an intrametastatic lymphatic vessel (PROX1, black). (**C**) High-power view of an intrametastatic lymphatic vessel with podoplanin$^+$ lymphatic endothelial cells and PROX1-expressing nuclei (arrows). The vessel contains a tumor embolus and is surrounded by mononuclear inflammatory or tumor cells. (**D**) Keratin$^+$ tumor cell emboli (brown) within intrametastatic lymphatic vessels with podoplanin$^+$ endothelial cells (red). (**E**) Large tumor embolus completely filling the lumen of an intrametastatic lymphatic vessel. (**F**) Aggregate of keratin$^+$ carcinoma cells disrupts an intrametastatic lymphatic vessel that is outlined by a single line of PROX1$^+$ nuclei (red). The margins of the vessel's rupture are indicated by green arrows. (**G** and **H**) Embolic tumor cell clusters (black arrows) within a branched intrametastatic lymphatic vessel, and a focal disruption of the lymphatic vascular wall by a bulk of aggregated tumor cells (green arrow). The lymphatic vessel's walls are composed of a single endothelial layer. Scale bars: 100 μm; 25 μm (insert).

example, in mammary carcinomas. This well-established fact is reflected in clinically validated and diagnostically indispensable consensus systems used in routine histopathological mammary tumor staging (10, 11). Testing these hypotheses, which are not mutually exclusive, depends on better understanding of the so-far elusive molecular mechanisms that determine the initial tumor cells' specific preference for invasion of blood or lymphatic vessels to reach their respective target organs.

Here we have systematically analyzed the lymphometastatic properties of human mammary carcinomas. These have distinct advantages for such studies, including the anatomically conserved lymphatic draining patterns of the human breast (12) and their repetitive pattern of metastatic spreading. Thus, most mammary carcinomas form their initial metastasis in up to 3 axillary lymph node or nodes that receive afferent lymph from the tumor and peritumoral tissue and are designated as "sentinel lymph nodes." Further metastatic progression occurs by successive colonization of the postsentinel lymph nodes in the axillary basin. Previous work has shown that lymphangiogenesis in sentinel lymph node metastases correlates with postsentinel tumor spreading (13). In this study, we have addressed the mechanisms underlying this process, using immunohistochemistry with selective lymphatic endothelial markers (podoplanin, LYVE1, and PROX1) (14–16), in vitro models, and xenograft tumors. The findings are compatible with a context-specific reaction of lymphatic endothelial cells with tumor-derived products of lipoxygenases that is critical for tumor cell entry into the lymphatic vessel and metastatic spreading from the sentinel to postsentinel lymph nodes. The results also shed light on the fact that different tumor types use different means to invade intrametastatic lymphatics.

Results

Intrametastatic lymphatic carcinosis. We localized lymphatic endothelial cells in 104 precisely matched primary ductal and lobular mammary carcinomas (stages pT1c, N0, or N1a, or pooled stages N2 and N3; ref. 11 and Supplemental Table 1; supplemental material available online with this article; doi:10.1172/JCI44751DS1) and in their corresponding sentinel and postsentinel axillary lymph nodes (Figure 1). Lymphatic vessels were restricted to the peritumoral stroma (17) in all the primary carcinomas. In contrast, the sentinel lymph node metastases of these tumors were often endowed with lymphatic vessels connected to those in the residual sentinel lymph node's parenchyma (Supplemental Figure 1). Their endothelial cells expressed the major lymphatic markers FLT4 (VEGFR3), podoplanin, PROX1, and, with some variability, also LYVE1, as reported (18). The density of intrametastatic lymphatics and their endothelial mitotic rate were more than 2-fold higher than those in residual lymph nodes (Supplemental Figure 2). The metastatic tumor cells were a major source of the lymphangiogenic factors

Table 1
Characterization of tumors and patients' outcome

pN Stage	Primary tumor stage pT1c diameter	Peritumoral carcinosis primary tumor	Grading	Grading (%)	Intrametastatic carcinosis	Local recurrence	Distant organ metastasis	Death	Follow-up period (months)
Ductal carcinoma									
pN1a a (n = 39)	1.8 ± 0.4 cm	19 (49%)	G1	2 (5%)	0 of 39 (0%)	0	5 (13%)	3 (8%)	54
			G2	22 (56%)					
			G3	15 (39%)					
pN2/3 (n = 20)	1.9 ± 0.3 cm	16 (65%)	G1	3 (15%)	20 of 20 (100%)	2 (10%)	5 (25%)	5 (25%)	56
			G2	8 (40%)					
			G3	9 (45%)					
Lobular carcinoma									
pN1a (n = 17)	1.9 ± 0.35 cm	4 (24%)	G1	0	0 (0%)	0	0	0	55
			G2	14 (82%)					
			G3	3 (18%)					
pN2/3 (n = 12)	1.8 ± 0.6 cm	5 (42%)	G1	0	6 of 12 (50%)	1 (8%)	3 (25%)	3 (25%)	57
			G2	10 (83%)					
			G3	2 (17%)					

Mean age, 58.9 ± 12.8 years. pT1c, primary tumors with diameters between 1–2 cm; pN1a, metastasis in 1–3 axillary lymph node(s), at least 4 larger than 2 mm in greatest diameter; pN2/3, metastases in more than 4 (ipsilateral) lymph nodes, at least 1 larger than 2 mm in greatest diameter. Data applies to all 3 tumor grades.

VEGFC and VEGFA (19), and their expression in the metastasis frequently exceeded that of the corresponding primary tumors (Supplemental Figure 3) and that of mononuclear cells (20) in the adjacent residual lymph node parenchyma or in naive lymph nodes (data not shown). These results suggest that metastatic tumor colonies provide lymphangiogenic factors and coopt the sentinel lymph node's premetastatic lymphatics and extend them by intrametastatic lymphangiogenesis.

We identified carcinoma cell emboli of various sizes within the intrametastatic lymphatic vessels of sentinel lymph nodes (Figure 1). Emboli were present in 100% (20 of 20) of ductal carcinomas with postsentinel lymph node involvement (Table 1), similar to our recent findings in extramammary Paget carcinomas (21). Strikingly, intrametastatic carcinosis was also present in all postsentinel lymph node metastases from individuals with advanced disease (data not shown). In contrast, lymphatic carcinosis was not detected in any of the 56 individuals in whom metastatic tumors were restricted to the sentinel lymph node (Table 1). After mean follow-up of 4.5 years, distant organ metastasis and death were more frequent in the patient group with (25%, 5 of 20 patients) than without intrametastatic lymphatic carcinosis (8%, 3 of 39 patients). The primary tumor's peritumoral lymphatic carcinosis was (statistically nonsignificantly) increased with the incidence of intrametastatic tumor emboli (Table 1). No further correlation of intrametastatic lymphatic carcinosis with luminal, basal, or ERBB2-overexpressing carcinoma subtypes (22) was observed. However, in contrast to ductal carcinomas, we found intrametastatic lymphatic carcinosis only in 50% (6 of 12) of lobular carcinomas with postsentinel lymph node involvement (Table 1). This is in line with previous results showing that the global gene expression of ductal and lobular subtypes differs significantly (23).

Using oligonucleotide arrays, we identified several gene products (DUSP1, RGS1, CYR61, CXCR4, and VEGFC) that were overexpressed in tumor cells of the metastasis compared with primary tumors, and the same discriminatory "markers" were also differentially expressed in intrametastatic lymphatic tumor emboli (Supplemental Figure 4). This indicates that tumor emboli originate from the surrounding metastasis rather than from the primary tumor directly via lymphatics in the premetastatic lymph node.

Bulk invasion of tumor cells into intrametastatic lymphatics. Due to the high density of intrametastatic lymphatics, we frequently observed that tumor cells aggregated into clusters and penetrated in bulk through large discontinuities of the intrametastatic lymphatic's walls (Figure 1). Tumor cell aggregates are located within the vascular lumen, and the vascular walls that border the discontinuity consist of a single endothelial cell layer. This is documented by localization of PROX1 that forms a single "rosary"-like cover around the tumor cells (Figure 1). These histological features are not compatible with surrounding and engulfment of the tumor cell clusters by newly formed lymphatic vessels that would result in a double layer of endothelial cells. Our results favor the interpretation of a direct penetration of the tumor cell aggregates through ruptures in the vascular wall that is also in line with the recent ex vivo observation obtained by video microscopy (24).

An in vitro model of lymphatic invasion. We used an in vitro coculture system to analyze the mechanisms of tumor cell–mediated disruption of lymphatic vessels. This employed spheroids (25, 26) of MCF7 mammary carcinoma cells to reproduce the clusters of cells seen in tumor emboli in vivo. MCF7 cell spheroids remained stable

Table 2
Overexpression of genes in MCF-7 spheroids versus monolayers

Description	Gene	Spheroid/monolayer	*P* value
Gain			
CD44 (Indian blood group)	*CD44*	3.45	0.0039
Intercellular adhesion molecule 1 (CD54)	*ICAM1*	2.67	0.0012
Vascular endothelial growth factor (VEGFA)	*VEGFA*	2.73	0.0100
Selectin L (lymphocyte adhesion molecule 1)	*SELL*	2.45	0.0055
Thrombospondin 2	*THBS2*	2.30	0.0125
Arachidonate 15-lipoxygenase	*ALOX15*	1.89[A]	0.0397
Cadherin 1 type 1, E-cadherin (epithelial)	*CDH1*	1.80	0.0139
Integrin alpha 5 (fibronectin receptor)	*ITGA5*	1.76	0.0370
Loss			
Laminin beta 1	*LAMB1*	–3.87	0.0133
Collagen type XII, alpha 1	*COL12A1*	–4.21	0.0016
Platelet/endothelial cell adhesion molecule (CD31)	*PECAM1*	–1.95	0.0041
Thrombospondin 1	*THBS1*	–1.91	0.0008
Vascular endothelial growth factor C (VEGFC)	*VEGFC*	–1.81	0.0295
Vitronectin	*VTN*	–1.45	0.0559

MCF7 cells were grown as spheroids or as monolayers, and lysed to extract and reverse transcribe RNA for low density arrays (Human Extracellular Matrix and Adhesion Molecules PCR Array; SABiosciences). Genes were identified that are differentially induced or repressed by MCF7 cell spheroid formation and could be related to bulk-like invasion through the lymphatic vasculature. [A]Corresponding gene products were studied in more detail.

for more than 6 hours. When aggregated into spheroids, MCF7 cells changed their gene expression patterns when compared with monolayers and increased their expression of CD44, ICAM1, and VEGFA; they also reduced their expression of matrix components (Table 2). Confluent monolayers of freshly isolated or telomerase "immortalized" (27) human dermal lymphatic endothelial cells were used as surrogates for intrametastatic lymphatics. We found no difference between intra- and extratumoral dermal lymphatics for the expression of several proteins (podoplanin, PROX1, FLT4, biglycan, endoglin, VE-cadherin, variably CD34, and LYVE1) (Supplemental Figure 4), justifying their use for the in vitro studies.

MCF7 spheroids were placed on top of lymphatic endothelial monolayers (Figure 2), which resulted in the highly reproducible formation of circular discontinuities that we designated as circular chemorepellent-induced defects (CCID) in monolayers precisely underneath the MCF7 spheroids. They were highly reminiscent of the defects seen in the lymphovascular walls at sites of tumor cell invasion in vivo. Lymphatic endothelial cells were more than 5 times more sensitive to MCF7 spheroid–induced CCID formation than blood vessel endothelia. CCID formation was not seen using spheroids of the nontumorigenic mammary gland epithelial cell line MCF-10A or human lung fibroblasts (HLFs) (Figure 2).

CCIDs form by migration of lymphatic endothelial cells. Time-lapse videos revealed centrifugal migration of lymphatic endothelial cells strictly beneath the MCF7 spheroids (Figure 2 and Supplemental Video). This correlated also with rearrangement and fragmentation of VE-cadherin in lymphatic endothelial cell junctions at the border of MCF7 spheroid–induced CCIDs (Figure 2). The migratory phenotype of the lymphatic endothelia was confirmed by the localization of the cell movement–associated activated protein phosphatase 1 regulatory inhibitor subunit 12 A (PPP1R12A, MYPT1) (ref. 28 and Figure 2). We discounted a role for apoptosis of lymphatic endothelial cells in the formation of CCIDs by TUNEL and Hoechst 33258 staining both in vitro and in vivo in human sentinel metastases (Supplemental Figure 5).

12(S)-HETE induces CCIDs in lymphatic endothelial cell monolayers. Oligonucleotide array analyses revealed the specific induction of several genes in MCF7 cell spheroids when compared with monolayers, including the hypoxia inducible (29) enzyme 15-lipoxygenase-1 (ALOX15) (Table 2), which metabolizes arachidonic acid to 12[S]-hydroxy-eicosatetraenoic acid (12[S]-HETE) and 15(S)-hydroxyeicosatetraenoic acid (15[S]-HETE). In humans, 12(S)-HETE is produced by ALOX15 and ALOX12, which are the respective products of the *ALOX15* and *ALOX12* genes (30). We have found that MCF7 cells only express *ALOX15* (Table 2), and it was shown previously that they lack *ALOX15B* (31). 12(S)-HETE was identified as a tumor cell–derived retraction factor for blood vessel endothelial cells (32). In lymphatic endothelial monolayers, 12(S)-HETE also transiently reduced VE-cadherin expression (Figure 2). These results fostered the speculation that 12(S)-HETE might be involved in MCF7-induced CCID formation.

We inhibited the enzymatic activity of ALOX15 in MCF7 cells by pharmacologic inhibition with the pan-LOX inhibitor nordihydroguaiaretic acid (33), which resulted in a significant and dose-dependent reduction of MCF7 spheroid–induced CCID areas in lymphatic endothelial cell monolayers (Supplemental Table 2). This result was confirmed with the LOX inhibitor baicalein (34) at nontoxic concentrations (Figure 3 and Supplemental Figure 6), which reduced CCID formation by 90% after 2 hours, and by 40% to 60% after 6 hours of coincubation as determined in pilot experiments (26).

Direct proof for the hypothesis that 12(S)-HETE triggered CCIDs was obtained by placing fibroblast spheroids soaked with synthetic 12(S)-HETE onto lymphatic endothelial cell monolayers. This resulted in CCID formation similar to that induced by MCF7 spheroids, whereas fibroblast spheroids imbibed with 15(S)-HETE or solvent were ineffective (Figure 3). Conversely, blocking 12(S)-HETE with a specific polyclonal antibody (35) inhibited the formation of MCF7 spheroid–induced CCIDs (Figure 3).

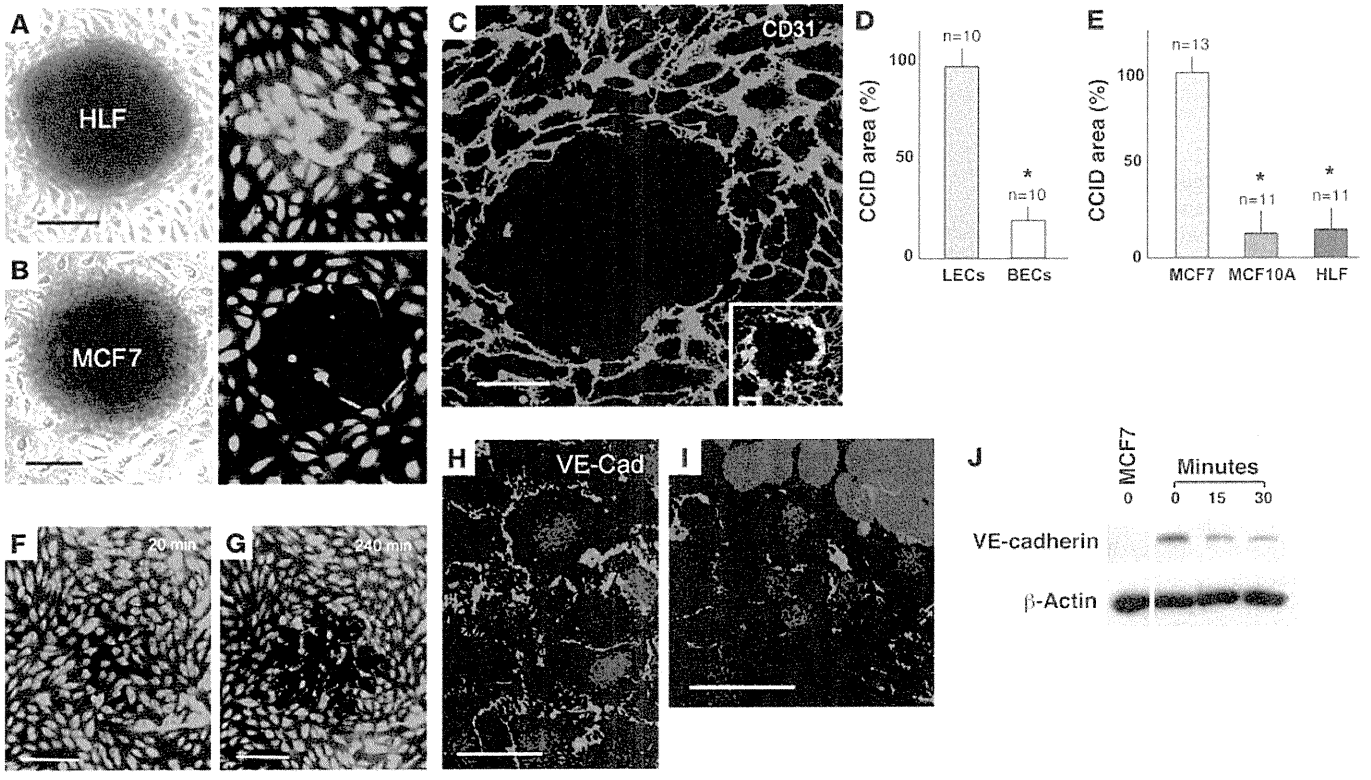

Figure 2

MCF7 cell spheroids induce CCIDs in lymphatic endothelial cell monolayers and disrupt VE-cadherin at the CCIDs. (**A**) Spheroid of HLFs fails to induce any defects in a monolayer of human lymphatic endothelial cells (LECs, Cytotracker tagged in green) after 4 hours of cocultivation. (**B**) MCF7 spheroids induce circular CCIDs. (**C**) A MCF7 spheroid–induced CCID is outlined when the LEC borders are stained for CD31 (red, confocal image). Inset, LECs (demarcated with CD31 in red) at the margin of the CCIDs show expression of PPP1R12A (MYPT1) (green) indicating cell mobility (confocal image). (**D**) MCF7 spheroids induce CCIDs preferentially in LEC monolayers (left bar), but significantly less (14.3% of lymphatics; $*P = 0.0047$) in monolayers of microvascular blood endothelial cells (BECs, right bar). (**E**) When compared with spheroids of MCF7 cells (left bar, 100%), CCID formation in lymphatic monolayers is marginally induced by nonmalignant human breast epithelial cells MCF-10A (9.6% of MCF7 spheroids), and HLFs (11.3%). Data are presented as mean ± SEM. $*P < 0.0001$. (**F** and **G**) Tracings of LEC migration (red lines; starting positions are marked by circles) beneath a spheroid during a 4-hour coincubation. (**H**) Confocal image shows continuous LEC junctions of VE-cadherin (VE Cad) at distance from a spheroid. (**I**) At the spheroid's margin, the VE-cadherin pattern is disrupted. (**J**) Confluent LECs were incubated with 1 μM 12(S)-HETE for 15 and 30 minutes or with solvent (0), and cell lysates were immunoblotted with antibodies to VE-cadherin or β-actin. As controls, VE-cadherin$^-$ MCF7 cells were used. Lanes were run on the same gel but are noncontiguous. Scale bars: 100 μm (**A**, **B**, **F**, and **G**); 25 μm (**C**); 50 μm (**H** and **I**).

These results indicated that CCIDs were induced by MCF7 cell spheroids, which were placed onto the upper side of the lymphatic endothelial monolayer that presumably corresponds to the luminal endothelial aspect in vivo. Here we show that CCIDs were also generated when the MCF7 spheroids were placed onto the basolateral aspects of lymphatic endothelial cells in Transwell chambers (Figure 4).

CCIDs were also obtained with spheroids of tumor lines other than MCF7 cells. This was found for human mammary carcinoma cells (HCC1419, HCC1443, and MDA-MB231) and colon cancer (LS174CoCa, HT29, HTC116), melanoma (CRL1675), and pancreatic adenocarcinoma (PANC1) (Figure 3).

Pharmacological inhibition of cognate mechanisms of tumor invasion and metastasis revealed a minor contribution of metalloproteinases since the pan-matrix-metalloprotease inhibitor GM6001 (36, 37), and specific inhibition of MMP9, TIMP2, and MMP2 reduced CCID formation only by approximately 25%. Reactive oxygen species and cyclooxygenases and their products were not involved (Supplemental Table 2).

Inhibition of 15LOX reduces CCID formation in lymphatic monolayers. Further evidence for the central role of *ALOX15* in CCID formation was obtained by shRNA-mediated knockdown in MCF7 cells (MCF7/*ALOX15*$^-$ cells), which resulted in stable reduction of over 80% of *ALOX15* mRNA as well as 12(S)-HETE and 15(S)-HETE production (Figure 5). Nonmalignant human MCF-10A cells or fibroblasts failed to induce CCIDs, to express *ALOX15* and *ALOX12* genes, and to synthesize 12(S)-HETE (Figure 5). Spheroids of MCF7/*ALOX15*$^-$ cells induced small CCIDs that were similar to baicalein-treated MCF7 spheroids, whereas controls (scrambled shRNA or empty vector–transfected MCF7 cells) were similar to unmodified MCF7 cells. This inhibitory effect of *ALOX15* shRNA was further enhanced by the pan-metalloprotease inhibitor GM6001 (Figure 5). Knocking in of *ALOX12* into MCF7/*ALOX15*$^-$ cells (Supplemental Figure 7) fully reestablished their CCID-forming capacity in the spheroid assay (Figure 5).

Reduced metastatic capacity of ALOX15-deficient tumor cells. We used MCF7 cells with transgene expression of VEGFC (MCF7/*VEGFC* cells) (38, 39) to induce metastasis formation in vivo. Both

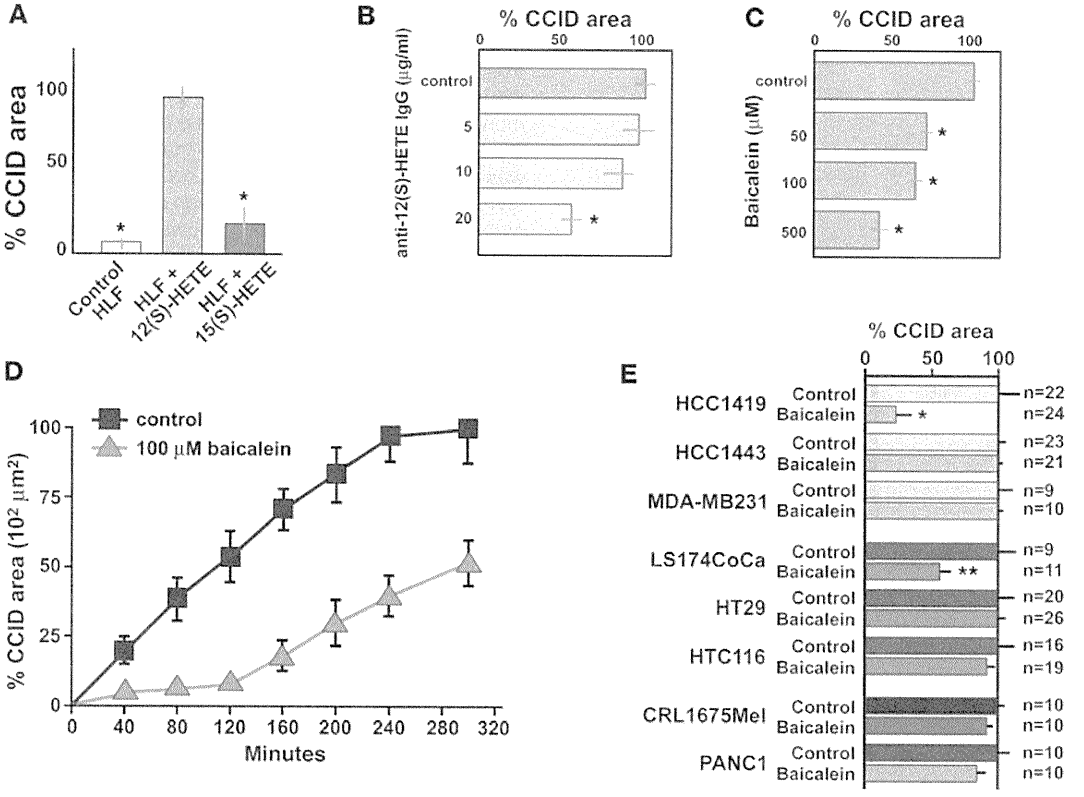

Figure 3

12(S)-HETE causes CCIDs in lymphatic endothelial cell monolayers. (**A**) CCID area in lymphatic endothelial cell monolayers induced by HLF cell spheroids that were presoaked with synthetic 12(S)-HETE ($n = 11$), 15(S)-HETE ($n = 12$), or solvent alone (control; $n = 21$). 12(S)-HETE induced approximately 20 times larger CCIDs than controls (*$P < 0.0001$) after 4 hours of coincubation. (**B**) Antibody against 12(S)-HETE reduces the CCID area by approximately 50% (*$P = 0.0020$). (**C**) The ALOX inhibitor baicalein, a traditional Asian anti-cancer drug, reduces CCID area in a dose-dependent fashion, with the highest dose of 500 μM ($n = 11$) causing reduction to 38% (*$P < 0.0001$) of controls ($n = 20$). (**D**) Time-course incubation over 4 hours with 100 μM baicalein in the media results in approximately 90% reduction of CCID size in the first 2 hours and a gradual increase in CCID formation to more than 50% after 4 hours. (**E**) Spheroids made of the mammary carcinoma cell lines HCC1419, HCC1443, and MDA-MB231 form spheroids that induce CCIDs in lymphatic monolayers, but only HCC1419 cell–mediated CCID formation is sensitive to 100 μM baicalein (inhibition of 78.2%; *$P = 0.0008$). Similarly, spheroids formed from colorectal carcinoma cell lines LS174CoCa, HT29, and HTC116 form CCIDs, but only LS174CoCa are baicalein sensitive (inhibition of 53.3%; **$P = 0.0168$). A melanoma (CRL1675Mel) and a pancreatic carcinoma cell line (PANC1) formed CCIDs in monolayers of lymphatic endothelial cells, but were insensitive (i.e., statistically not significant) to baicalein. All data are presented as mean ± SEM.

VEGFC-overexpressing and unmodified MCF7 cells expressed *ALOX15* and formed CCIDs of similar size in lymphatic monolayers (Supplemental Figure 8). Stable transfection with luciferase (MCF7/*VEGFC/luc*) did not interfere with the expression of other transgenes (data not shown). MCF7/*VEGFC/ALOX15*$^-$*/luc* or control MCF7/*VEGFC/luc* cells that contained scrambled shRNA were injected orthotopically into mammary fat pads of SCID mice. After 32 days, tumors had formed in 100% of animals injected with control MCF7 cells, but only in 50% with MCF7/*VEGFC/ALOX15*$^-$ cells, presumably due to a less receptive micromilieu at the sites of injection, which showed minimal inflammatory infiltration in all cases. However, once established, the xenograft tumors of all MCF7/*VEGFC* cell variants showed similar growth rates, tumor cell turnover, weights, and intratumoral lymphatic vascular densities (Figure 6). At 32 days, 60% of animals in the control groups, but none of the mice bearing MCF7/*ALOX15*$^-$ xenograft tumors, had developed regional lymph node metastases (Figure 6). Sixty-three days after injection, we found lymph node metastases in 100% of control mice, but only in 5% of the MCF7/*ALOX15*$^-$ group. At this end point, the weight of all primary xenograft tumors was similar, and the expression of *VEGFC* transgene and the *ALOX15* shRNA knockdown were unaltered (Figure 6). In xenograft tumors induced by cells of the *ALOX15*-expressing control groups, podoplanin$^+$ and LYVE1$^+$ intratumoral lymphatic vessels had formed that were distended and focally obliterated by tumor emboli at 32 days after injection (38, 39). In contrast, tumors composed of MCF7/*VEGFC/15LOX*$^-$ cells developed collapsed intratumoral lymphatic vessels that were devoid of embolic tumor cells (Figure 6). These in vivo results support the concept that *ALOX15*-driven production of 12(S)-HETE is required for formation of lymph node metastases, by facilitating the entry of tumor cells into intrametastatic lymphatic vessels.

ALOX15 and 12(S)-HETE in human metastases. The relevance of our experimental findings for the formation of human postsentinel lymph node metastases was underscored by immunohistochemical localization of 12(S)-HETE and of ALOX15 in metastatic carcinoma cells in sentinel lymph nodes (Figure 7). This was extended and confirmed by further analysis of tissue arrays containing cores of primary tumors and their corresponding sentinel metastases from

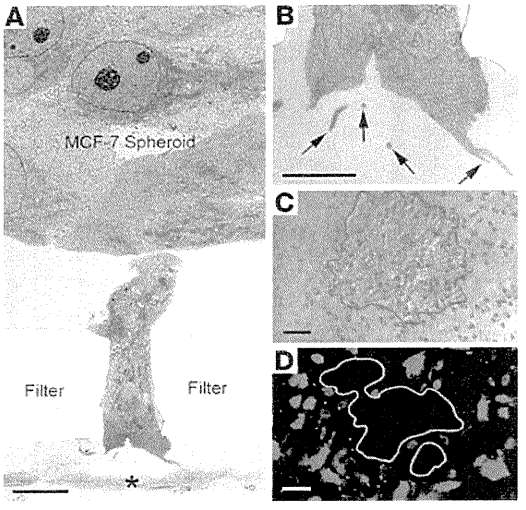

Figure 4
MCF7 tumor cell induced CCID formation in lymphatic monolayers from the abluminal side in Transwell inserts. MCF7 cell spheroids were placed onto the upper side of a filter that was covered by an LEC monolayer on its lower side so that the spheroids were separated from the lymphatic endothelial cells by the filter membrane. Coincubation was performed for 12 hours. (**A**) Low-power electron micrograph of a spheroid extending a "finger" through a filter pore. The LEC monolayer at the basal aspect of the filter shows only extracellular material and debris (*). (**B**) Higher magnification of the tip of the spheroid's extension, showing microvillar or vesicular (arrow) membrane structures, resembling shedding microparticles. (**C**) A spreading spheroid of MCF7 cells (outlined in red) on the upper face of the Transwell membrane. (**D**) At the opposite basal (abluminal) side of the Transwell membrane, a CCID (outlined in green) is formed in the monolayer of lymphatic endothelial cells (tagged red) precisely corresponding to the MCF7 spheroid on the luminal side. Scale bars: 1 μm (**A**); 0.2 μm (**B**); 50 μm (**C** and **D**).

13 patients with ductal carcinomas. These samples were precisely matched for staging pT1c and pN1a. Scoring of immunostaining for ALOX15 (Figure 7) provided evidence for a link between enzyme expression in lymph node metastases and the time of metastasis-free survival, and thus clinical outcome. A similar trend was also observed for the expression of ALOX12 (Supplemental Figure 9).

Discussion

The number of axillary lymph nodes that host metastases of mammary carcinomas is of predictive clinical significance. In this study, we have gained insights into the potential cellular and molecular events involved in metastatic tumor progression from the sentinel to the postsentinel axillary lymph nodes in human mammary carcinomas. This process involves premetastatic conditioning of axillary lymph nodes, invasion of tumor cells into the interconnecting lymphatic vessels, and eventually intranodal tumor cell arrest and proliferation.

Tumors programmed for lymph node metastasis have acquired a specific strategy for premetastatic adaptation of their regional lymph nodes (40, 41), which prominently involves expansion of lymph node sinus and transformation of their lining cells into lymphatic endothelia. This reaction is a stereotypic response to diverse stimuli that range from chemokines and growth factors to lymph congestion by mechanical obliteration of efferent lymphatic vessels (42, 43). However, it is of importance for formation of lymph node metastases and is referred to as *premetastatic lymph node lymphangiogenesis* (41). Moreover, lymphatic vessels develop de novo within the lymph node's metastatic colony and are frequently embolized by tumor cells that phenotypically correspond to cells of the metastasis and not to those in the primary tumors. Intrametastatic lymphangiogenesis occurs in all cases with postsentinel metastasis, and it is also present when the tumor is restricted to the sentinel lymph node. However, only when tumor cells have invaded and embolized the intrametastatic lymphatics do they spread to further lymph nodes downstream, as documented by a 100% correlation of embolization with postsentinel lymph node metastasis, which also applies to further tumor spreading from postsentinel metastases into more distal axillary lymph nodes. This also implies that the intrametastatic lymphatics are connected to the lymph node's efferent lymphatic vessels and is in line with recent experimental evidence (44). Collectively, these results indicate that tumor cell invasion of intrametastatic lymphatic vessels is crucial for lymphatic metastatic tumor dissemination.

These results raise the question of how the tumor cells get access into the intrametastatic lymphatic vasculature. Several pathways of tumor invasion into lymphatic vessels have been observed for different experimental and human tumors (45). One variant implies single tumor cell penetration between or even through endothelial cells, possibly also involving tumor cell epithelial-mesenchymal transition (21, 46, 47). In this investigation, we provide evidence for another pathway for mammary carcinomas similar to that previously described (45), which involves bulk invasion of metastatic tumor cells through large discontinuities of the lymphatic vessel wall. This pathway matches with recent experimental results obtained by in vivo microscopy in which xenografted mammary carcinoma cells spontaneously form mobile cohesive groups that preferentially invade into lymphatic vessels (24).

To gain insights into the mechanisms underlying lymphatic bulk invasion, we have adapted a reductionistic in vitro assay (25, 26) that mimics some features of the in vivo situation. In this system, tumor cell spheroids corresponded to invasive tumor aggregates in vivo, and in lieu of intrametastatic lymphatic vessels, we used monolayers of dermal lymphatic endothelial cells. This choice of endothelial cells was justified because a panel of typical lymphatic genes, including PROX1 and podoplanin, was expressed equally in both normal dermal and intrametastatic lymphatic endothelial cells. In contrast, we have noted that MCF7 cells altered their gene expression program upon spheroid formation and that this includes overexpression of the 12(S)-HETE–producing enzyme ALOX15. The human gene project has revealed 2 *ALOX* isoforms, *ALOX15* and *ALOX15B*. ALOX15B produces 15(S)-HETE only, and there is no evidence that it plays a role in breast cancer pathology (48, 49). In contrast, ALOX15 also generates 12(S)-HETE, which is of relevance for various cancers, including mammary carcinomas (50).

12(S)-HETE was previously shown to increase malignant behavior of some tumors and to reduce it in others (51), and to increase endothelial cell motility and retraction of human umbilical cord endothelial cells (52). This has prompted us to investigate the role of 12(S)-HETE in our in vitro surrogate system of tumor bulk invasion. Our results show that 12(S)-HETE released by MCF7 tumor spheroids induced CCIDs that were formed by centrifugal migration of lymphatic endothelial cells just beneath spheroids. It is possible that this local restriction of endothelial cell mobility could be due to the hydrophobicity

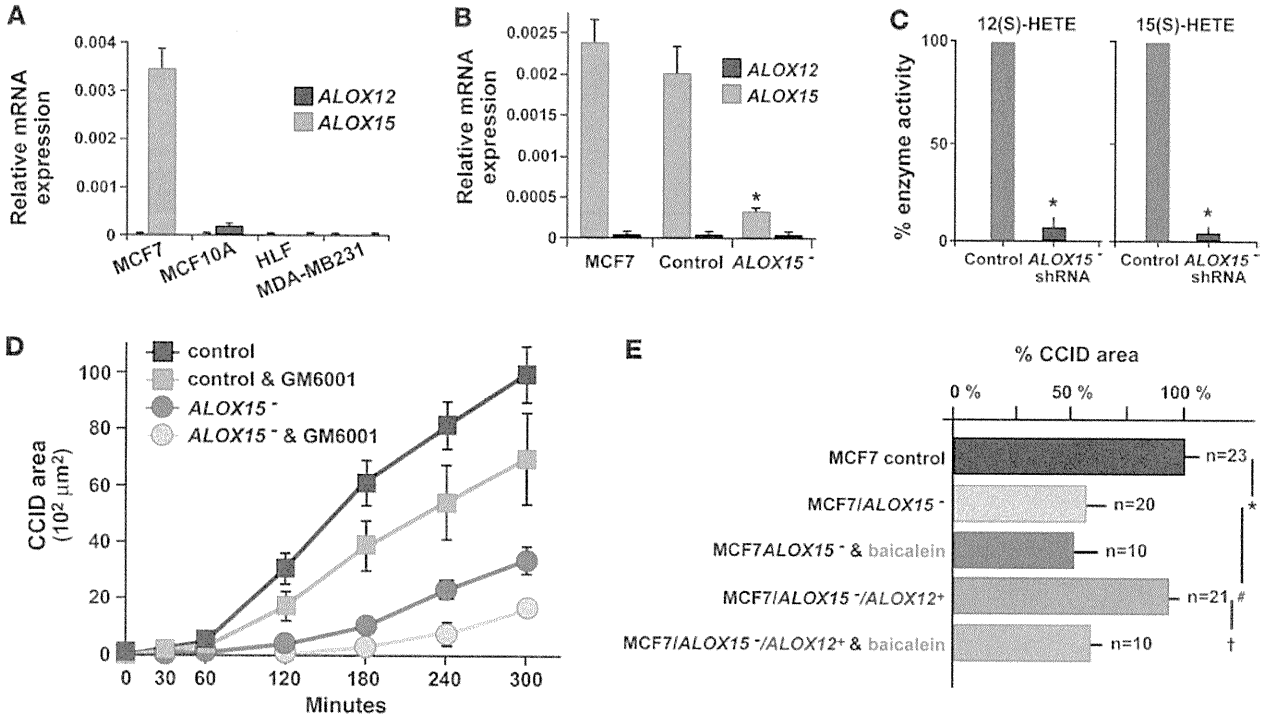

Figure 5

shRNA-mediated knockdown and rescue of lipoxygenase in MCF7 cells. (**A**) The expression of mRNAs of *ALOX15* and *ALOX12* was determined by real-time PCR in MCF7 and MDA-MB231 mammary carcinoma cells and in controls (noncancerous breast epithelial cells MCF-10A and HLFs). MCF7 cells express only *ALOX15* mRNA, but not *ALOX12* mRNA, whereas all other cells fail to produce any of the tested *ALOXs*. (**B**) mRNA levels of *ALOX15* were determined in unmodified MCF7 cells, in control MCF7 cells transduced with scrambled shRNA, and in MCF7/*ALOX15*$^-$ cells. Knockdown of *ALOX15* reduced the expression of *ALOX15* mRNA significantly (*P = 0.0009 compared with vector control) when compared with unmodified or control transduced MCF7 cells. (**C**) Production of 12(S)-HETE and 15(S)-HETE, the arachidonic acid metabolites of ALOX15, is reduced by more than 90% in MCF7/*ALOX15*$^-$ cells when compared with control MCF7 cells that were transduced with scrambled shRNA (*P > 0.0001). (**D**) shRNA-mediated knockdown of *ALOX15* in MCF7 cells (blue line) causes a size reduction similar to that of baicalein in CCID (compare to Figure 3D). This is further aggravated by coincubation with 20 μM of the pan-metalloprotease inhibitor GM6001 (yellow line), which had a similar effect (green line) on controls (MCF7 cells transduced with scrambled shRNA, red line). (**E**) Reconstitution of CCID-forming activity of MCF7/*ALOX15*$^-$ cells by transfection with *ALOX12*. MCF7 spheroid–induced CCID formation is analyzed in the presence or absence of 100 μM baicalein. There is a significant difference in CCID size between MCF7/control versus MCF7/*ALOX15*$^-$ spheroids (*P = 0.0017), MCF7/*ALOX15*$^-$ versus MCF7/*ALOX15*$^-$/*ALOX12*$^+$ spheroids (#P = 0.0249), and MCF7/*ALOX15*$^-$/*ALOX12*$^+$ spheroids ± baicalein treatment (†P = 0.0331). All data are presented as mean ± SEM.

of 12(S)-HETE that could be released in poorly diffusing membrane microvesicles above its critical micellar concentration (53). However, the actual concentration of 12(S)-HETE in the micromilieu at the spheroid tumor endothelial interface remains to be determined (54). 12(S)-HETE was not toxic for lymphatic endothelial cells, and accordingly, we failed to encounter apoptotic endothelial cells in association with CCIDs. The significance of 12(S)-HETE was confirmed by blocking of CCID formation by a specific antibody or by shRNA-mediated knockdown of the producing enzyme ALOX15. The ability to cause CCIDs was restored by knocking in of *ALOX12*, which also produces 12(S)-HETE and is not expressed in MCF7 cells. 15(S)-HETE, the alternative arachidonic acid metabolite produced by ALOX15, was ineffective. CCID formation was further supported by metalloproteases that loosen the meshwork of VE-cadherin at interendothelial junctions and matrix attachment (36, 37). Taken together, our in vitro findings suggested a hitherto unknown dominant role for ALOX15 and its product 12(S)-HETE in tumor cell–lymphatic endothelial cell interaction. When we extrapolate these in vitro findings to the vascular defects we have observed at sites of tumor cell bulk invasion, it is possible that induction of lymphatic endothelial migration and focal disruption of interendothelial adhesion (e.g., by destabilization of VE-cadherin) could contribute to focal openings in the vascular wall.

Intriguingly, blood endothelial cells were much less sensitive to the migration-inducing effect of 12(S)-HETE than lymphatics. It remains to be determined whether or not this is due to differences in receptor- or nonreceptor-mediated effects. So far, several proteins have been implicated in binding of 12(S)-HETE; however, a definitive universal receptor or receptors are still elusive. We have screened for the expression of 2 putative 12(S)-HETE membrane protein receptors — the leukotriene B_4 receptor (55) and the orphan receptor GPR31 (56) (data not shown) — and failed to detect expression differences between blood and lymphatic endothelial cells. Thus, our results show that 12(S)-HETE preferentially caused CCID formation in lymphatic endothelial monolayers, either by direct interaction with so-far elusive lymphatic receptor or receptors, or indirectly, via currently unidentified intermediaries.

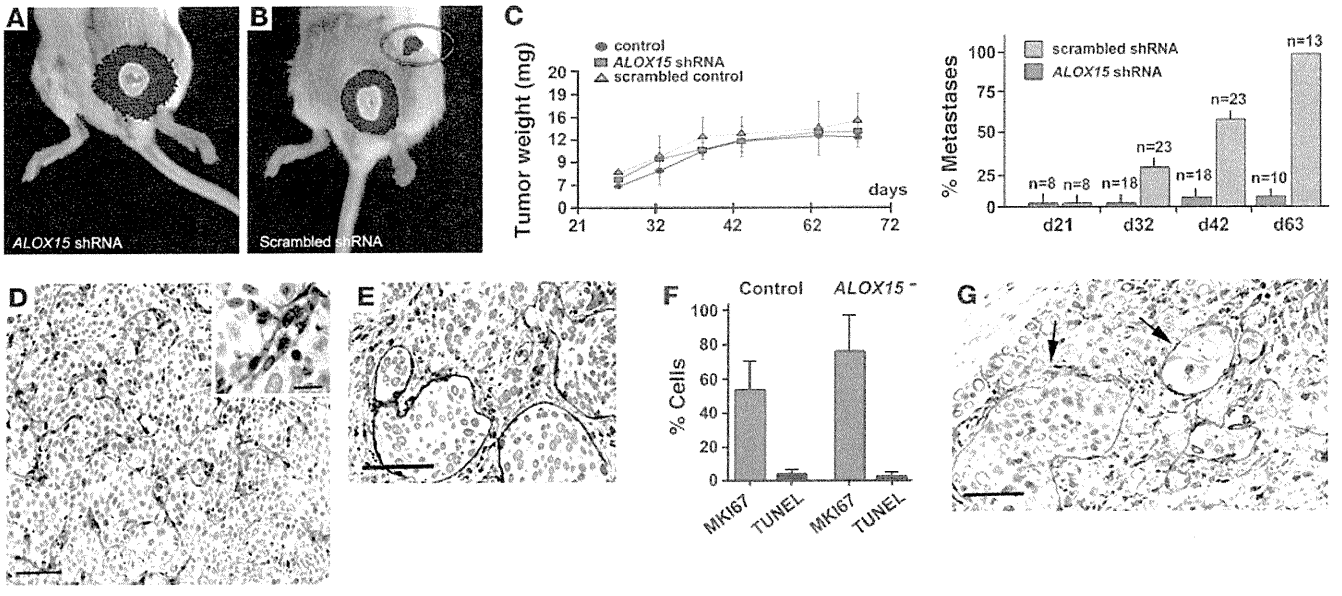

Figure 6

Xenograft tumors induced by *ALOX15* shRNA knockdown cells and control MCF7/*VEGFC* cells expressing luciferase as reporter. (**A**) Bioluminescence image of a xenograft tumor induced by cells that lack *ALOX15* after injection into the fifth mammary fat pad failed to develop lymph node metastases after 32 days. (**B**) Image of a xenograft tumor induced by control MCF7/*VEGFC* cells that were transfected with scrambled shRNA and expressed *ALOX15*, showing a regional lymph node metastasis (red circle). (**C**, left panel) The sizes and growth rates of all xenograft tumors, irrespective of the nature of the inoculated tumor cells (MCF7/*VEGFC*, or MCF7/*VEGFC* cells transfected with scrambled or *ALOX15* shRNA) were similar. (**C**, right panel) Time course of metastasis formation of xenograft tumors induced by MCF7/*VEGFC* cells transfected with *ALOX15* shRNA (red) or with control scrambled shRNA (green) showing that *ALOX15*-deficient MCF7/*VEGFC* were incompetent of metastasis formation. (**D**) Representative picture of a xenograft tumor (same as depicted in **A**). The tumor cells fail to invade into the collapsed intratumoral podoplanin$^+$ lymphatic vessels (red). Insert, tumor embolus–free intratumoral lymphatic vessel with a narrow lumen. (**E** and **G**) Xenograft tumor of the control group (same as in **B**) showing massive tumor intravasation into dilated lymphatic vessels (arrows) that were immunostained for LYVE1 (**E**) or podoplanin (**G**). (**F**) Growth rates of xenograft tumor MCF7/*VEGFC* and MCF7/*VEGFC*/*ALOX15*$^-$ cells were determined by labeling for MKI67 (Ki-67) or by the TUNEL assay. Image analysis revealed a higher (but not significant) MKI67 positivity in *ALOX15*$^-$ tumors compared with control tumors. The rate of apoptosis was similar in both primary tumor types. $n = 6$. Total number of counted nuclei was greater than 2000. Scale bars: 70 μm (**D**, **E**, and **G**); 20 μm (inset). All data are presented as mean ± SEM.

Our results apply primarily to ductal mammary carcinomas that are represented in vitro by MCF7 and HCC1419 cells derived from estrogen receptor–positive ductal carcinomas of the luminal subtype (57). However, only 50% of the lobular mammary carcinomas followed this pattern of tumor spreading. Baicalein-insensitive CCIDs were formed by MDA-MB321 and HCC1443 mammary carcinoma cells that are derived from estrogen receptor–negative ductal carcinomas of the basal subtype and lack ALOXs. This is in contrast to our findings in human tumors and could be due to changes induced by in vitro culturing. Furthermore, the CCID assay suggested that tumors derived from other organs apparently use LOX-independent mechanisms. These include most colorectal carcinomas, melanomas, and a pancreatic cancer. Thus, there is no universal mechanism by which different types of tumors form and propagate lymph node metastases. They apparently also have at their disposal ALOX15-independent mechanisms to enter lymphatic vessels and do not use bulk but rather single-cell invasion, with or without epithelial-mesenchymal transition, possibly depending on TGF-β (24).

These results required verification in a tumor xenograft model that mimics the key findings in sentinel lymph node metastases, i.e., formation of intratumoral lymphatic vessels, bulk invasion of tumor cells, lymphatic embolization, and formation of lymph node metastases. A suitable model for this in vivo proof of principle was found in mouse xenograft tumors produced by human mammary carcinoma MCF7 cells that transgenically overexpress VEGFC (38, 39). This transforms MCF7 cells from nonmetastatic into highly metastatic, with intratumoral lymphangiogenesis, lymph vessel invasion, and embolization, i.e., analogous to human sentinel lymph node metastases. Moreover, we found that MCF7 cells express only a single lipoxygenase, *ALOX15*, and are thus ideally suited for studying the contribution of this enzyme to CCID. shRNA-induced knockdown of *ALOX15* efficiently repressed formation of lymph node metastases. Intratumoral lymphatic vessels were induced both in the control and the *ALOX15* knockdown xenografted tumors. However, in ALOX15-deficient tumors, the lymphatics were collapsed and empty and tumor cells failed to invade and form emboli, in striking contrast to *ALOX15*-expressing and 12(S)-HETE–producing control MCF7 cells. However, we cannot exclude the possibility that the absence of LOX products alters the lymphatic endothelial phenotype to make it less permissive to tumor cell invasion in general.

Here we have brought together 3 correlative observations, i.e., the embolization and invasion of mammary carcinoma cells into intrametastatic lymphatics in human tissues, the 12(S)-HETE–driven formation of CCIDs in vitro, and the important role of the 12(S)-HETE–producing enzyme, ALOX15, for lymph node metastasis formation in mouse xenograft models.

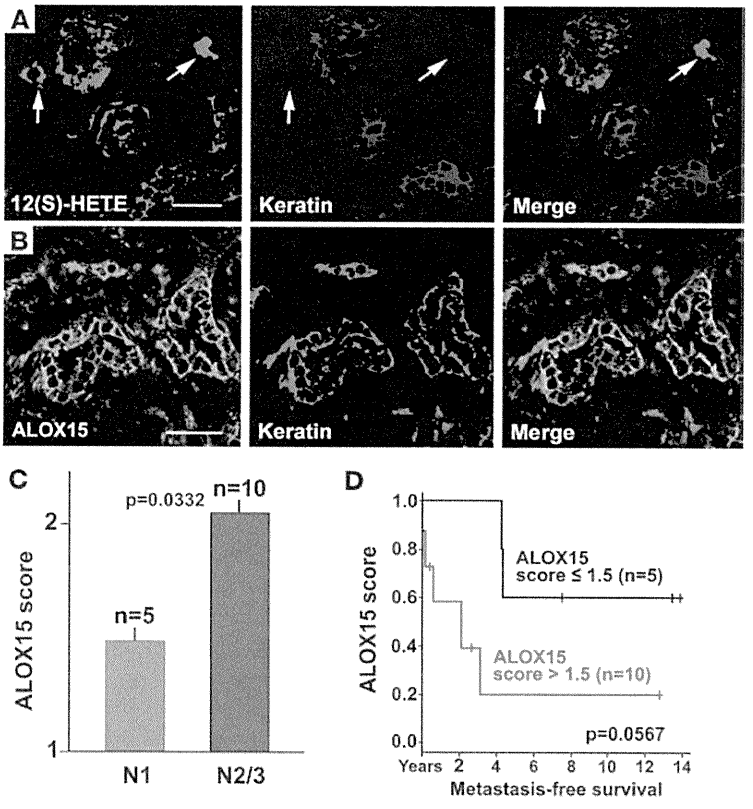

Figure 7
12(S)-HETE and ALOX15 in human sentinel metastases. (**A**) Localization of 12(S)-HETE (red) in the mammary carcinoma cells in a representative sentinel lymph node of a patient with postsentinel lymph node metastasis (total examined: n = 12). 12(S)-HETE colocalizes with tumor cell keratin (blue and merge) and is also expressed by nontumor, presumably inflammatory cells (arrows). (**B**) The 12(S)-HETE–producing enzyme ALOX15 shows a localization similar to that of its product (ALOX15: green; keratin: red). (**C**) Results of the tissue array scoring of the immunostaining for ALOX15 in the tumor cells of the sentinel metastasis in 15 cases of ductal carcinoma. In 5 cases without postsentinel metastases, the score is lower (N1, green column) than in 10 cases with postsentinel spreading (N2/3, red column). (**D**) Metastasis-free survival correlates inversely with the expression of ALOX15 in the tumor cells of the sentinel lymph nodes (P = 0.0507). Scale bars: 50 μm. All data are presented as mean ± SEM.

Taken together, these complementary results favor the hypothesis that 12(S)-HETE–mediated CCID formation is a central event for accession of mammary carcinoma cells into the lymphatic vasculature in sentinels and thus furthers tumor spreading into postsentinel lymph nodes (Supplemental Figure 10).

Do these potential mechanisms of intrametastatic lymphatic invasion also apply to human patients? Our results suggest that this is feasible. Metastatic tumor cells in sentinel lymph nodes of human mammary carcinomas express all the key players, ALOX12, ALOX15, and 12(S)-HETE. In feasibility studies using tissue microarrays of a relatively small number of carefully matched human samples, we found that the abundance of ALOXs is inversely correlated with metastasis-free survival. Pharmacological ALOX inhibition has previously been recognized as antimetastatic and proapoptotic (58, 59) therapy for mammary and other carcinoma cells. Here we show the CCID-reducing efficiency of the ALOX inhibitor baicalein (34), a polyflavone isolated from the roots of *Scuttelaria baicalensis* and still applied in traditional Asian medicine. Thus, our findings could hold the potential that inhibition of ALOX interferes with lymphatic dissemination of ductal mammary carcinomas. Formal clinical studies are required to determine whether or not ALOXs in mammary carcinomas can be used as biomarkers and potential therapeutic targets.

Methods

Selection of cases and tissue samples. Use of human tissue samples and experimental mouse models was approved by the Ethical Committee of the Medical University of Vienna (Approval EK-Nr 270/2006) in compliance with Austrian legislation. We have selected 104 archival cases of mammary carcinomas, classified as NOS, with 69 cases of ductal and 35 of lobular subtype. The patients had not received preoperative neoadjuvant therapy. The primary tumors were matched by their diameters (pT1c, 1–2 ± 0.6 cm), availability of the sentinel, and, when clinically indicated, also postsentinel axillary lymph nodes. Further inclusion criteria were similar sizes of sentinel lymph node metastases (pN1a, >2 mm) and documented follow-up periods of 55 months after surgery. The tumor grading is listed in Table 1. The tumors were also subclassified by immunohistochemistry as luminal, basal, or ERBB2 enriched (22). Sentinel lymph nodes were free of tumors (stage pN0, n = 16) (11), or metastasis was restricted to the sentinel lymph node only (pN1a, n = 56), or also involved additional postsentinel axillary lymph nodes (pN2 or 3, n = 32). All tumors were analyzed for the expression of estrogen and progesterone receptors, the overexpression of ERBB2, and in some cases also for keratins, CD133, CD44, and aldehyde dehydrogenase (60, 61). As controls, naive nontumor-associated lymph nodes were used that were removed during carotid angioplasty or abdominal surgery (n = 16). These nonactivated lymph nodes were devoid of capsular fibrosis, intranodal scars, or activation of germinal centres.

Immunohistochemistry. 4-μm-thick freshly prepared sections from archival paraffin blocks for immunolabeling were processed as described previously (62) using rabbit anti-human podoplanin IgG (5 μg/ml) or with a monoclonal mouse IgG (Bender Med Systems BMS 1105; 1 μg/ml), and anti-human PROX1 rabbit IgG (AngioBio). Some sections were also incubated after podoplanin labeling with monoclonal mouse anti-Ki67 IgG (MIB-1) or anti-human LYVE1 rabbit IgG (DAKO). Rabbit antibodies to 12(S)-HETE (Assay Designs), with less than 2.5% cross-reactivity with 12(R)-HETE and less than 0.3% with 15(S)- and 5(S)-HETE, and ALOX12 and ALOX15 (Abcam) were used on cryostat sections of unfixed primary carcinomas and their sentinel metastases (n = 12). For immunofluorescence, we used appropriate secondary antibodies labeled with Alexa Fluor 488, Alexa Fluor 594, or Alexa Fluor 633 (Molecular Probes). Double-labeling experiments were controlled

by omitting the primary antibodies or by replacement with irrelevant antibodies raised in the same species or of the same mouse IgG subtype. The densities of lymphatic vessels were determined in duplicate by 3 independent observers on unmarked histological sections. We counted the number of lymphatic vessel profiles in at least 30 microscopic fields for each slide, using an objective lens with ×25 magnification. Inter- and intra-observer variations resulted in a "background noise" of 1 vessel per field, and only counts above this threshold were entered into the evaluation. Statistical significance was determined by the *t* test, using the Prism 4 software package (GraphPad). Production and composition of tissue microarrays were performed as described (63). We have carefully selected 15 cases of ductal carcinomas with the identical stages pT1c, pN1a ($n = 10$), and pT1c, pN2/3 ($n = 5$).

Isolation and characterization of human dermal lymphatic endothelial cells. Human lymphatic endothelial cells and blood vessel endothelial cells were prepared from commercial (C-12260; PromoCell) or freshly prepared dermal microvascular endothelial cells by sorting with anti-podoplanin and anti-CD31 IgG using Dynabeads (M-280; Dynal 11203) or FACS (FaxStar), as described (64). Also, telomerase "immortalized" lymphatic endothelial cells were used (27). No differences in the expression of other proteins previously thought to distinguish lymphatic vessels outside and within tumors (biglycan, endoglin, CD34, VE-cadherin) were found (Supplemental Figure 4C).

Determination of 12(S)-HETE. 12(S)-HETE and 15(S)-HETE were determined by a reverse-phase high-performance liquid chromatography method (RP-HPLC), as described (65).

Spheroid preparation. Cell spheroids were prepared as described in preliminary experiments (25, 26). Briefly, MCF7 cells were grown in McCoy 5A medium containing 10% fetal calf serum and 1% penicillin/streptomycin (Gibco-BRL; Invitrogen). Noncancerous MCF-10A breast epithelial cells were grown in MEGM medium (CC-3150; Clonetic Bullet Kit) supplemented with bovine pituitary extract, human epithelial growth factor, hydrocortisone, insulin, 1% penicillin/streptomycin, and 10 μM isoproterenol. Normal HLFs were grown in nonessential amino acid media containing 10% fetal calf serum and 1% penicillin/streptomycin and 1% nonessential amino acids.

Low-density real-time PCR arrays. Template cDNAs prepared from total RNA of MCF7 cells grown as monolayer or spheroid were characterized in triplicates using the Human Extracellular Matrix and Adhesion Molecules PCR Array (SABiosciences) and the RT2 SYBR Green/Fluorescein qPCR Master Mix (SABiosciences) on the Chromo4 PCR System (Bio-Rad), following the manufacturer's instructions. The resulting Ct values were analyzed by using the RT2 Profiler PCR Array Data Analysis Template v3.2 (SABiosciences). Genes not included on the low-density real-time array were analyzed by using the following FAM probes obtained from Applied Biosystems: *VEGFA* Hs00173626_m1, *ALOX15* Hs00609608_m1, *ALOX12* Hs00167524_m1, and *ALOX12B* Hs00153961_m1.

MCF-7 spheroid/LEC monolayer cocultivation. In all experiments, telomerase-"immortalized" lymphatic endothelial cells (27) or freshly prepared lymphatic endothelial cells (64) (maximal 6 passages) were used, with identical results. Lymphatic endothelial cells were seeded in EGM2MV medium on 24-well plates and allowed to grow to confluence. Then, the lymphatic endothelial cells (LECs) monolayers were stained with Cytotracker green (2 μg/ml, C2925; Molecular Probes) or Hoechst 33258 (5 μg/ml, H1398; Sigma-Aldrich) at 37°C for 90 minutes. Into each well, 10 MCF7 spheroids were transferred. During the coincubation period, frames were taken at 15-minute intervals with an inverse fluorescence microscope (Zeiss Axiophot) and composed to a time-lapse video. Some preparations were examined in a Zeiss confocal fluorescence microscope.

Transwell culture. Primary or telomerase-immortalized lymphatic endothelial cells were grown on the lower surface of Transwell inserts (membrane diameter 6.5 mm; pore size 8 μm, precoated with 10 μg/ml fibronectin; Costar) until confluent. Then lymphatic endothelial cells were stained with Cytotracker as described above, and tumor cell spheroids were placed onto the upper surface. Coculturing was performed for 24 hours, with fluorescence microscopic control of the LEC monolayer every 180 minutes.

Analysis of CCID formation. Areas of LEC monolayers beneath spheroids were photographed in an Axiovert (Zeiss) fluorescence microscope, using the FITC filter to visualize Cytotracker-stained (green) lymphatic endothelial cells, and the area of CCIDs was measured using Axiovision software (Zeiss).

shRNA knockdown of ALOX15. Lentiviral particles containing shRNA targeting the human *ALOX15* mRNA (SHCLNV-NM_001140) and controls with nonsense shRNA (SHC002V) were obtained from Sigma-Aldrich. MCF7 cells that transgenically overexpress *VEGFC* (38) were seeded onto 24-well plates, and transduced with 2e5 TU in 250 μl MEM containing 10% FCS and 8 μg polybrene/ml by spin infection at 1500 *g* at 32°C for 90 minutes. After incubation for 12 hours, the cells were reseeded onto 100-mm culture plates and selected with 1 μg/ml puromycin for 1 week. Single-cell colonies were tested for knockdown efficiency by real-time PCR, normalizing gene expression to the housekeeping gene *GAPDH*.

Knockin of ALOX12 cDNA. N-terminal *V5*-tag was fused to the *ALOX12* full-length cDNA. The fusion was constructed by PCR (5′ primer: TCAGATCCGCTAGCGGGCGCCATGGGTAAGCCTATCCCTAACCCTCTCCTCGGTCTCGATTCTACGGGCCGCTACCGCATCCGCGTGGCCA, 3′ primer: GGTGGCGGCGGCCGCTCAGATGGTGACACTGTTCTCTATGCAGCTGGG) using standard PCR conditions and an *ALOX12*-containing expression plasmid (gift from Brigitte Marian, Cancer Research Institute, Vienna, Austria) as template. The primer pair contained 5′ Nhe-I and 3′ Not-I linkers and the PCR product was directly subcloned into pTag-CFP-N (Evrogen) by replacing CFP with the tagged fusion construct. The resulting vector DNA was controlled by sequencing and proper expression of the target gene by Western blotting with a *V5*-tag antibody (Invitrogen) using total lysates of transfected cells.

Xenograft tumors. For xenografting, 10^7 MCF7 cells or their derivatives were dispersed in 30 μl PBS and injected orthotopically into the fat pads of the fifth mammary glands of 8-week-old female SCID mice (Harlan Animal Research Laboratory). 60-day slow-release pellets containing 0.72 mg of 17β-estradiol (Innovative Research of America) were implanted 48 hours previously. Primary tumor growth and formation of metastases were monitored at 10-day intervals by noninvasive bioluminescence imaging using a highly sensitive CCD camera (IVIS 100; Caliper Life Sciences). 150 μg D-luciferin/g of body weight (firefly, potassium salt; Caliper Life Sciences) was injected intraperitoneally. Bioluminescence signals were acquired 18 minutes after application, and normalized signals (photons/sec/cm²/sr) were evaluated and quantified using Living Image Software (Caliper Life Sciences); the tumor weight was calculated from a calibration curve. The experiment was terminated after 63 days, and primary tumors and lymph node metastases were processed for anti-podoplanin immunohistochemistry or for mRNA determination of *VEGFC*, *ALOX12*, and *ALOX15*, shRNAs, and luciferase. Paraffin sections of formalin-fixed tissues were labeled by the TUNEL assay (Chemicon), MKI67 (KI-67, Novo Castra NCL-Ki67p), and cytokeratin (DAKO Z0622). Fluorescence microscopy was performed on an Axiophot microscope equipped with an AxioCam Colour camera (Zeiss) at a standard magnification of 250. Images were analyzed using ImageJ software package 1.42q (Wayne Rasband, NIH; http://rsb.info.nih.gov/ij).

Statistics. We have used a 2-tailed *t* test for statistical analysis of the experimental data. $P \leq 0.05$ was considered significant. All data are presented as mean ± SEM. The human correlative data were expressed by Kaplan-Meier statistics.

Acknowledgments

This work was supported in part by European Community project LSHG-CT-2004-503573 (Lymphangiogenomics) (to D. Kerjaschki and K. Alitalo); a research fund from the Keyaki-kai Medical Corporation, Tokyo, Japan (to H. Nosaka); by the GenAU project Drug Action by Genomic Networks (DRANGON) (to V. Sexl); by Fonds für Innovative und Interdisziplinäre Krebsforschung der Gemeinde Wien (to G. Krupitza); and by the Austrian Breast and Colorectal Cancer Study Group (ABCSG) (to M. Gnant and M. Rudas). We thank A. Rees for reading the manuscript and A. Jaeger for help with the graphic work.

Received for publication August 13, 2010, and accepted in revised form February 2, 2011.

Address correspondence to: Dontscho Kerjaschki, Clinical Department of Pathology, Allgemeines Krankenhaus Wien, Medical University of Vienna; Waehringer Guertel 18-20, A 1090 Vienna, Austria. Phone: 431.40400.5176; Fax: 431.40400.5193; E-mail: dontscho.kerjaschki@meduniwien.ac.at.

Gregor Bartel's present address is: Department of Internal Medicine III, Medical University of Vienna, Vienna, Austria.

Veronika Sexl's present address is: Department of Pharmacology, Veterinary Medical University, Vienna, Austria.

Hitonari Nosaka's present address is: Department of Internal Medicine, Teikyo University, Tokyo, Japan.

Monika Hämmerle's present address is: Department of Pathology, University of Heidelberg, Heidelberg, Germany.

Helmut Dolznig's present address is: Department of Medical Genetics, Medical University of Vienna, Vienna, Austria.

1. Fidler IJ. The pathogenensis of cancer metastasis: the "seed-and-soil" hypothesis revisited. *Nat Rev Cancer*. 2003;3(6):453–458.
2. Psaila B, Lyden D. The metastatic niche: adapting the foreign soil. *Nat Rev Cancer*. 2009;9(4):285–293.
3. Metha P. Potential role of platelets in the pathogenesis of tumor metastasis. *Blood*. 1984;63(1):55–63.
4. Tammela T, Alitalo K. Lymphangiogenesis: Molecular mechanisms and future promise. *Cell*. 2010; 140(4):460–476.
5. Eyles J, et al. Tumor cells disseminate early, but immunosurveillance limits metastatic outgrowth, in a mouse model of melanoma. *J Clin Invest*. 2010;120(6):2030–2039.
6. Müller-Hermelink N, et al. TNFR1 signaling and IFN-gamma signaling determine whether T-cells induce tumor dormancy or promote multistage carcinogenesis. *Cancer Cell*. 2008;13(6):507–518.
7. Tait CR, Dodwell D, Horgan K. Do metastases metastasize? *J Pathol*. 2004;203(1):515–518.
8. Norton L, Massagué J. Is cancer a disease of self-seeding? *Nat Med*. 2006;12(8):875–878.
9. Ben-Porath I, et al. An embryonic stem cell-like gene expression signature in poorly differentiated aggressive human tumors. *Nat Genet*. 2008; 40(5):499–507.
10. Carlson RW, et al. Breast cancer. Clinical practice guidelines in oncology. *J Natl Compr Canc Netw*. 2009;7(2):122–192.
11. Sobin LH, Gospodarowicz MK, Wittekind C, eds. *TNM Classification of Malignant Tumours (Uicc International Union Against Cancer)*. New York, New York, USA: Wiley-Blackwell; 2009.
12. Britton TB, Solanki CK, Pinder SE, Mortimer PS, Peters AM, Purushotham AD. Lymphatic drainage pathways of the breast and the upper limb. *Nucl Med Commun*. 2009;30(6):427–430.
13. Van den Eynden G, et al. Increased sentinel lymphnode lymphangiogenesis is associated with non-sentinel axillary lymph node involvement in breast cancer patients with a positive sentinel node. *Clin Cancer Res*. 2007;13(18 pt 1):5391–5397.
14. Breiteneder-Geleff S, et al. Angiosarcomas express mixed endothelial phenotypes of blood and lymphatic capillaries: podoplanin as a specific marker for lymphatic endothelium. *Am J Pathol*. 1999;154(2):385–394.
15. Banerji S, et al. LYVE1, a new homologue of the CD44 glycoprotein, is a lymph-specific receptor for hyaluronan. *J Cell Biol*. 1999;144(4):789–801.
16. Wigle JT, Oliver G. Prox1 function is required for the deveLOXpment of the murine lymphatic system. *Cell*. 1999;98(6):769–778.
17. Marinho VF, Metze K, Sanches FS, Rocha GF, Gobbi H. Lymph vascular invasion in invasive mammary carcinomas identified by the endothelial lymphatic marker D2-40 is associated with other indicators of poor prognosis. *BMC Cancer*. 2008;8:64.
18. Van den Eynden GG, et al. Induction of lymphangiogenesis in and around axillary lymph node metastases of patients with breast cancer. *Br J Cancer*. 2006;95(10):1362–1366.
19. Hirakawa S, Kodama S, Kunstfeld R, Kajiya K, Brown LF, Detmar M. VEGFA induces tumor and sentinel lymph node lymphangiogenesis and promotes lymphatic metastasis. *J Exp Med*. 2005;201(7):1089–1099.
20. Schoppmann SF, et al. Tumor-associated macrophages express lymphatic endothelial growth factors and are related to peritumoral lymphangiogenesis. *Am J Pathol*. 2002;161(3):947–956.
21. Hirakawa S, et al. Nodal lymphangiogenesis and metastasis: Role of tumor-induced lymphatic vessel activation in extramammary Paget's disease. *Am J Pathol*. 2009;175(5):2235–2248.
22. Sotiriou C, et al. Breast cancer classification and prognosis based on gene expression profiles from a population-based study. *Proc Natl Acad Sci U S A*. 2003;100(18):10393–10398.
23. Bertucci F, et al. Lobular and ductal carcinomas of the breast have distinct genomic and expression profiles. *Oncogene*. 2008;27(40):5359–5372.
24. Giampieri S, Manning C, Hooper S, Jones L, Hill CS, Sahai E. Localized and reversible TGFbeta signalling switches breast cancer cells from cohesive to single cell motility. *Nat Cell Biol*. 2009; 11(11):1287–1296.
25. Offner FA, et al. Interaction of human malignant melanoma tumor spheroids with endothelium and reconstituted basement membrane: modulation by RGDS. *Int J Cancer*. 1993;54(3):506–512.
26. Madlener S, et al. Multifactorial anticancer effects of digalloyl-resveratrol encompass apoptosis, cell cycle arrest, and inhibition of lymphendothelial gap formation in vitro. *Br J Cancer*. 2010;102(9):1361–1370.
27. Schoppmann SF, et al. Telomerase-immortalized lymphatic and blood vessel endothelial cells are functionally stable and retain their lineage specificity. *Microcirculation*. 2004;11(3):261–269.
28. Matsumura F, Hartshorne DJ. Myosin phosphatase target subunit: Many roles in cell function. *Biochem Biophys Res Commun*. 2008;369(1):149–156.
29. Hultén LM, et al. 15-Lipoxygenase-2 is expressed in macrophages in human carotid plaques and regulated by hypoxia-inducible factor-1alpha. *Eur J Clin Invest*. 2010;40(1):11–17.
30. Funk CD. The molecular biology of mammalian lipoxygenases and the quest for eicosanoid functions using lipoxygenase-deficient mice. *Biochim Biophys Acta*. 1996;1304(1):65–84.
31. Subbarayan V, et al. Inverse relationship between 15-lipoxygenase-2 and PPAR-gamma gene expression in normal epithelia compared with tumor epithelia. *Neoplasia*. 2005;7(3):280–293.
32. Honn KV, et al. Tumor cell-derived 12(S)-hydroxyeicosatetraenoic acid induces microvascular endothelial cell retraction. *Cancer Res*. 1994; 54(2):565–574.
33. Funk CD. Lipoxygenase pathways as mediators of early inflammatory events in atherosclerosis. *Arterioscler Thromb Vasc Biol*. 2006;26(6):1204–1206.
34. Li-Weber M. New therapeutic aspects of flavones: the anticancer properties of Scutellaria and its main active constituents Wogonin, Baicalein and Baicalin. *Cancer Treat Rev*. 2009;35(1):57–68.
35. González-Núñez D, Claria J, Rivera F, Poch E. Increased levels of 12(S)-HETE in patients with essential hypertension. *Hypertension*. 2001;37(2):334–338.
36. Deryugina EI, Quigley JP. Matrix metalloproteinases and tumor metastasis. *Cancer Metastasis Rev*. 2006;25(1):9–34.
37. Baker AH, Edwards DR, Murphy G. Metalloproteinase inhibitors: biological actions and therapeutic opportunities. *J Cell Sci*. 2002;115(pt 19):3719–3727.
38. Karpanen T, et al. Vascular endothelial growth factor C promotes tumor lymphangiogenesis and intralymphatic tumor growth. *Cancer Res*. 2001;61(5):1786–1790.
39. He Y, et al. Vascular endothelial cell growth factor receptor 3-mediated activation of lymphatic endothelium is crucial for tumor cell entry and spread via lymphatic vessels. *Cancer Res*. 2005;65(11):4739–4746.
40. Ran S, Volk L, Hall K, Flister MJ. Lymphangiogenesis and lymphatic metastasis in breast cancer. *Pathophysiology*. 2010;17(4):229–251.
41. Mumprecht V, Detmar M. Lymphangiogenesis and cancer metastasis. *J Cell Mol Med*. 2009; 13(8A):1405–1416.
42. Steinmann G, Földi E, Földi M, Rácz P, Lennert K. Morphologic findings in lymph nodes after occlusion of their efferent lymphatic vessels and veins. *Lab Invest*. 2009;47(1):43–50.
43. Angeli V, et al. B cell-driven lymphangiogenesis